

MODELING AND PROCESS-STRUCTURE-PROPERTY-PERFORMANCE STUDY
OF PEROVSKITE SOLAR CELLS

by

SHOIEB SHAIK

DAWEN LI, COMMITTEE CHAIR
SUSAN BURKETT
MARGARET KIM
ARUNAVA GUPTA
LIN LI

A DISSERTATION

Submitted in partial fulfillment of the requirements
for the degree of Doctor of Philosophy in the
Department of Electrical and Computer Engineering
in the Graduate School of
The University of Alabama

TUSCALOOSA, ALABAMA

2017

Copyright Shoieb Shaik 2017
ALL RIGHTS RESERVED

ABSTRACT

This dissertation study mainly falls into two parts: simulation study and experimental investigation of the process-structure-property-performance relationship in perovskite solar cells.

Herein, a controllable fabrication of annealing-free perovskite films with tunable crystal grain size and morphology via a seeded approach has been developed. Specifically, a solution of lead iodide (PbI_2) was spin-coated on a substrate, and a low concentration solution of Methylammonium iodide (MAI) was dropped onto the PbI_2 film to form perovskite seed before introducing high concentration solution of MAI. The fast, annealing-free seeded nucleation and growth leads to dense and uniform perovskite thin films exhibited controllable crystal grains.

In another project, a polymer additive assisted approach to facilitate the growth of uniform, dense, and ultra-smooth perovskite thin films has also been demonstrated. In specific, a polymer, Polyamidoamine (PAMAM) dendrimers, was incorporated into the blend solution of lead iodide (PbI_2) and Methylammonium iodide (MAI) to regulate the nucleation and growth thereby tuning the morphology and crystallinity. The PAMAM addition not only realized compact perovskite thin films without pinholes in it, but also increased the stability.

In the simulation study, both the organic bulk heterojunction solar cells and perovskite solar cells have been systematically investigated to help understand the device operation and guide the experiments. Different electron transport layers (ETL) and hole transport

layers (HTL) were used to study the effect of band gap alignment with adjacent layers and improve the transport of charges. The change in band gap not only facilitated in collection of charges but also improved the overall power conversion efficiency (PCE) of the device in study. Recombination of charges in the bulk active region and its effect on overall PCE was also studied.

DEDICATION

This work is dedicated to my family and friends.

LIST OF ABBREVIATIONS AND SYMBOLS

HOMO	Highest occupied molecular orbital
LUMO	Lowest occupied molecular orbital
ETL	Electron transport layer
HTL	Hole transport layer
EBL	Electron blocking layer
HBL	Hole blocking layer
DSSC	Dye-sensitized solar cell
OSC	Organic solar cell
PSC	Perovskite solar cell
PVSK	Perovskite
SEM	Scanning electron microscopy
TEM	Transmission electron microscopy
XRD	X-ray diffraction
UV-vis	Ultraviolet visible spectroscopy
AFM	Atomic force microscopy
PV	Photovoltaic
PCE	Power conversion efficiency
Voc	Open-circuit voltage
Jsc	Short-circuit current

FF	Fill factor
ε	Permittivity
EF	Fermi level
k	Boltzmann's constant
ρ	Density of charge carriers (hole or electron)
q	Charge of charge carriers (hole or electron)
μ	Field-effect mobility
n	Electron density
p	Hole density
ITO	Indium tin oxide
MAPbI ₃	Methylammonium lead iodide
FAPbI ₃	Formamidinium lead iodide
CaTiO ₃	Calcium titanate
MAI	Methylammonium iodide
PEDOT: PSS	Poly(3,4-ethylenedioxythiophene) polystyrene sulfonate
TiO ₂	Titanium oxide
ZnO	Zinc oxide
Al ₂ O ₃	Aluminum oxide
Cs ₂ CO ₃	Cesium Carbonate
PC ₆₁ BM	Phenyl-C61-butyrac acid methyl ester
LiF	Lithium fluoride

CIGS	Copper indium gallium selenide
CdTe	Cadmium telluride

ACKNOWLEDGMENTS

Throughout the course of my PhD, I have received tremendous support from many people and they deserve my sincere thanks. First and foremost, I would like to thank my loving parents and my siblings for their unconditional love and support during my years as a graduate student. Next, I would like to thank my uncle Dr. Shaik Jeelani for his unconditional support and guidance throughout my graduate school. My aunt, Ms. Fatima Ahmad is a motherly figure and she has stayed with and guided me through all the achievements and hardships throughout my life. Dr. Shaik Zainuddin have helped me with research discussions and guided me through all the hurdles. Next, I would like to extend my sincere thanks to my research advisor Dr. Dawen Li (Associate Professor, Department of Electrical Engineering, University of Alabama). He has been a true mentor in every sense of the word. Not only he was a great mentor but an honest critic which has helped me develop tremendously in my academic and personal life as well. Dr. Li has been very patient with me and uplifted me through knowledgeable discussions and presentations.

My committee members, Dr. Arunava Gupta, Dr. Susan Burkett, Dr. Margaret Kim and Dr. Lin Li deserves my great gratitude for their valuable scientific discussion and suggestions.

I would like to thank Dr. Ziyou Zhou for his continuous support and discussions with my projects. Dr. Zhou has been a great friend and mentor.

I would like to give special thanks to my dear friend Dr. Muhammad Farooq for being there for me when I needed him the most. A special person, who deserves a mention here is Vaishali Batra. I am grateful to her for her continuous support and discussions in research collaborations. I would also like to give my special thanks to my friends Mr. Syed Hasson Basha, Dr. Harish Rao, Dr. Trupti Kotbagi, Dr. Abhishek Kumar, Dr. Abhay Lidbe, Dr. Archana Panikar, Dr. Neha Pachauri, Dr. Anurag Gupta, Ms. Sanchita Dhirwani and Dr. Prateeksha Premraj.

I would also like to thank CAF (central analytical facility) staff Mr. Johnny Goodwin, Mr. Rich Martens and Mr. Rob Holler for training me on the equipment and helpful discussions about microscopy.

CONTENTS

ABSTRACT	ii
DEDICATION.....	iv
LIST OF ABBREVIATIONS AND SYMBOLS	v
ACKNOWLEDGMENTS	viii
LIST OF TABLES.....	xii
LIST OF FIGURES	xiii
CHAPTER 1. INTRODUCTION.....	1
1.1 Hybrid Perovskite Solar Cells.....	2
1.2 Structure and Charge Transport Layers in Perovskite Solar Cells.....	4
1.3 Stability of Perovskite Solar Cells	7
1.4 Working Principle of Perovskite Solar Cells and Device Characterization.....	9
CHAPTER 2. SIMULATION STUDY OF PEROVSKITE SOLAR CELLS	13
2.1 Introduction.....	13
2.2 Influence of Different PCBM and Cathode Materials on PCE	15
2.3 Effect of P3HT Hole Mobility on Efficiency.....	18
2.4 PCE versus ITO Work Function	20
CHAPTER 3. SIMULATION STUDY OF ORGANIC POLYMER SOLAR CELLS	24

3.1 Introduction.....	24
3.2 Inverted Device Structure and Materials in Simulation.....	28
3.3 Optimization of Active Layer.....	30
3.4 Dependence of Optimal Thickness on Mobility and Recombination.....	31
3.5 Effect of Recombination.....	34
3.6 Effect of Hole Mobility in the Electron-donating Polymer.....	34
3.7 Electron Transport Layer Selection.....	35
CHAPTER 4. CONTROLLABLE GROWTH OF ANNEALING-FREE PEROVSKITE THIN FILMS VIA A SEEDED APPROACH.....	37
4.1 Experiments.....	48
CHAPTER 5. POLYMER ADDITIVE ASSISTED FABRICATION OF ULTRA- SMOOTH AND STABLE PEROVSKITE THIN FILMS.....	50
5.1 Rapid IR lamp annealing of perovskite thin films.....	57
5.2 Morphology and crystallization of perovskite thin films, and resulting performance of perovskite solar cells.....	62
CHAPTER 6. CONCLUSION AND FUTURE WORK.....	65
6.1 Conclusions.....	65
6.2 Future Work.....	66
REFERENCES.....	69

LIST OF TABLES

Table 1: Several representative devices performances of inverted planar structured perovskite solar cells.....	7
Table 2: Input parameters used for perovskite solar cell simulation	15
Table 3: Device performance with PCBM ETL and Al/ Ag cathode	17
Table 4: Device parameters for both ZnO and TiO ₂ electron transport layers	36
Table 5: Extracted device parameters from J-V characteristics in fig. 40.....	64

LIST OF FIGURES

Figure 1: Structure of hybrid AMX_3 perovskite crystals.....	3
Figure 2: Three typical device structures of perovskite solar cells: (a) mesoporous, (b) regular (n-i-p) planar structure, and (c) inverted (p-i-n) planar structure	4
Figure 3: (a) Schematic of inverted perovskite solar cell structure used in the project, (b) energy band diagram showing charge carrier transport and collection.	9
Figure 4: J-V curve of a solar cell	12
Figure 5: Simulation workflow of SETFOS for photovoltaic devices	13
Figure 6: Energy band diagram of perovskite solar cells with inverted structure of ITO/PEDOT/Perovskite/PCBM/Cathode. ETL layer is either $PC_{61}BM$ and $PC_{71}BM$ with Al or Ag cathode.....	16
Figure 7: Energy band diagram with P3HT as HTL in inverted perovskite solar cells.....	18
Figure 8: Effect of P3HT hole mobility on efficiency	19
Figure 9: Energy band diagram with PEDOT HTL and PCBM ETL	20
Figure 10: Efficiency vs ITO work function	21
Figure 11: Energy band diagram without PEDOT hole transport layer	22
Figure 12: Efficiency vs ITO work function	23
Figure 13: Schematic flow chart showing the steps converting sunlight to electricity in organic photovoltaics.....	25
Figure 14: Schematic of conventional (regular) polymer-fullerene bulk heterojunction solar cells. A blend of conjugated polymer with a fullerene derivative serves as active layer. A transparent conductive oxide (TCO) such as ITO acts anode, and a top metal electrode.....	26
Figure 15: Schematic of solar cell configuration for a) Regular structure: ITO (anode) glass/ PEDOT: PSS/ PCPDTBT: PC70BM/ Al (cathode) b) Inverted structure: ITO (cathode) glass/ ZnO/ PCPDTBT: PC70BM/ PEDOT: PSS/ Au (anode).....	27

Figure 16: Inverted organic solar cell configuration: ITO (cathode) glass/ ZnO/PCPDTBT: PCBM/ PEDOT: PSS/Au (anode)	29
Figure 17: Chemical structure of a) PCPDTBT polymer b) PC ₇₀ BM	30
Figure 18: a) Variation of efficiency, short-circuit current density and fill factor with active layer thickness b) Simulated J-V characteristics as a function of active layer thickness.	30
Figure 19: Dependence of optimal thickness on mobility and recombination a) PCE, J _{sc} , and FF versus thickness at increased mobility of $\mu_n = 6E-2 \text{ cm}^2/\text{Vs}$ and $\mu_p = 1E-3$ cm^2/Vs and constant recombination rate = 0.5; b) simulated J-V characteristics for parameter extraction of part a; c) PCE, J _{sc} , and FF versus thickness at reduced recombination rate of 0.1 and unchanged mobility of $\mu_n = 6E-3 \text{ cm}^2/\text{Vs}$ and $\mu_p = 1E-4$ cm^2/Vs ; and d) simulated J-V characteristics for parameter extraction of part c.	33
Figure 20: a) Effect of langevin recombination rate on PCE, J _{sc} , and FF, b) simulated J-V characteristics as langevin recombination rate varies.	34
Figure 21: a) effect of hole mobility on power-conversion efficiency, short-circuit current density and fill factor, b) simulated J-V characteristic curves with different hole mobility.....	35
Figure 22: Energy band diagram of PCPDTBT: PCBM based organic bulk heterojunction solar cells using a) ZnO and b) TiO ₂ as electron transport layer	35
Figure 23: Schematic illustration of seeded growth of perovskite thin films and device fabrication.....	38
Figure 24: Fig. 1 SEM images of a) the PbI ₂ film, b) the perovskite seed layer, c) the perovskite film obtained by seeded growth, d) high magnification image of perovskite film by seeded growth, e) the perovskite thin film obtained from the premixed PbI ₂ and MAI solution, and f) regular interdiffusion method without seeding layer.....	40
Figure 25: XRD patterns of PbI ₂ , PbI ₂ with perovskite seed, and the perovskite thin film formed by seeded growth. 3b) UV/Vis spectra of PbI ₂ , PbI ₂ with seed, perovskite thin film obtained by seeded growth with or without thermal annealing.	41
Figure 26: SEM images for first MAI layer optimization. For the second step of MAI, concentration was constant at 10 mg/mL. For the first step MAI, concentration was varied from 0.5 mg/mL (a & d), 1 mg/mL (b & e), 1.5 mg/mL (c), and 2 mg/mL (f), respectively.....	42
Figure 27: a) XRD patterns of perovskite thin film with different incubation time of PbI ₂ and first step MAI solution. b) grain size analysis by using Scherrer equation. The full width at half maximum at 33.6° was employed for the calculations.....	43

Figure 28: SEM images for the second MAI layer optimization First step of MAI, concentration was constant at 1 mg/mL Second step MAI, concentration varied from 10 mg/mL (a & d), 20 mg/mL (b & e), 30 mg/mL (c & f)	44
Figure 29: XRD patterns of PbI ₂ with seeding layers as a function of first step MAI solution sitting time. Without 2nd MAI)	45
Figure 30: Incubation time optimization for perovskite thin films Incubation time (low concentration MAI solution on top of PbI ₂ before spin-coating) dependent formation of perovskite thin film. a) 10s, b) 30s, c) 40s, d) 60s, and e) histogram of particle size of perovskite thin film determined from SEM images.	46
Figure 31: Performance of the perovskite device.	48
Figure 32: XRD patterns of perovskite thin films with different ratio of PAMAM (after annealing)	52
Figure 33: XRD patterns of PAMAM-perovskite thin films at different annealing time. The concentration of PAMAM was 4%.	53
Figure 34: SEM images of Perovskite-PAMAM thin films with different solvent wash: a1) a2) chlorobenzene, b1) b2) dichlorobenzene c1) c2) diethyl ether, d1) d2) toluene ...	54
Figure 35: XRD patterns of perovskite thin films with different solvent used for perovskite film washing.....	55
Figure 36: Optical images of the film degradation with different concentration of PAMAM.	56
Figure 37: Sample temperature versus lamp annealing time under 125 W lamp when placed on wood, metal and glass sample supporting plate.	60
Figure 38: Sample temperature versus lamp annealing time under 250 W lamp when placed on wood, metal and glass sample supporting plate.	61
Figure 39: (Left) SEM images show morphologies of perovskite thin films with IR lamp annealing. (a) 30 seconds for samples on wood plate, (b) 60 seconds also on wood plate, (c) 3 minutes on glass sample holder. (Right) Corresponding XRD spectra.....	62
Figure 40: Comparison of I-V characteristics between fast lamp annealing in less than 3 minutes.....	63

CHAPTER 1. INTRODUCTION

Although water, global warming, eradication of hunger and poverty, and health are some of the alarming issues that preventing human being from better living, energy is the most pivotal compulsion to govern and overcome the above-mentioned issues. The never-ending energy consumption to the daily requirements has driven the world running short of fossil fuels energy resources. Most of the energy consumption of the world is provided by fossil fuels (~80%). The rest is covered using coal (20.8%), natural gas (31.6%) and crude oil (22.3%)^[1]. Continued dependence on fossil fuels might lead to alarming increase in rate of CO₂ emission. As a renewable energy sources for electricity generation and power production, photovoltaics that convert endless solar energy to electricity could be a viable solution. Solar energy has potential as high as 23000 TW, implying by installing 10% efficient photovoltaic modules covering only 1% area on earth, today's global energy demands can be met. After enough investment and persistent study in photovoltaic field, the maximum capacity of photovoltaics reached only to a fraction of global energy needs (200 GW).

High-performance, cost effective solar cells for mass production could save the world in energy crisis, also greatly reduce the emission of greenhouse gas. Compared with solar cells based on inorganic semiconductors, such as Silicon and Gallium Arsenide, solution processable organic photovoltaics and perovskite solar cells have a great potential

to be produced in large quantities at comparatively lower costs because of abundant materials and their compatibility with roll-to-roll (R2R) printing.

1.1 Hybrid Perovskite Solar Cells

The existing photovoltaic technologies can be categorized into three generations. The first generation of solar cells is mainly comprised of crystalline silicon and is the most widely used technology for commercialization to date and cover up to 90% of the current market. Although the crystalline silicon based photovoltaic technology is widely used, these bulk silicon solar cells come with limitations in flexibility and energy consumption to produce high purity silicon ingots. Copper indium gallium selenide (CIGS) and cadmium telluride (CdTe) based thin film solar cells fall under the second generation of photovoltaics. CIGS and CdTe PV technologies cover remaining 10% of the photovoltaic market. These two kinds of solar cells have their limitations in mass production of telluride and indium. The presence of cadmium in CdTe can be detrimental to environment. Overall, first-generation and second-generation solar cells may not be a viable replacement for fossil fuels due to limitations in mass production and overcoming the cost barrier.

The third generation, which is also known as the emerging photovoltaic technology holds a strong potential to replace fossil fuels. Dye- sensitized cells (DSSC), organic solar cells (OSC), quantum dot cells, organic tandem solar cells and perovskite solar cells (PSC) fall under emerging photovoltaic technologies. Out of all these technologies, perovskite solar cells stand out as a strong contender because of their rapid progress in efficiency^[1]. Perovskite solar cells have reached to efficiencies up to 22% in

just a period of 6 years. In comparison, it has taken about 2 decades for silicon based technologies to reach the same power conversion efficiency.

The same crystal structure as calcium titanate (CaTiO_3), which was discovered by Russian scientist L.A. Perovski, the class of perovskite materials are represented as AMX_3 , where A is an organic cation, M is a metal cation and X is oxide or halide anion. The structure of a perovskite crystal is demonstrated in fig. 1. A large organic or molecular cation (positively charged) of type A is in the center of a cube. The metal cation M and halide anion X are arranged in MX_6 octahedral form and the center of the octahedral M is surrounded by halides X at the corners. The typical perovskite crystals are generally represented in a form of $\text{CH}_3\text{NH}_3\text{MX}_3$, where $\text{M} = \text{Sn}, \text{Pb}$ and $\text{X} = \text{Cl}, \text{I}, \text{or Br}^{[2-7]}$.

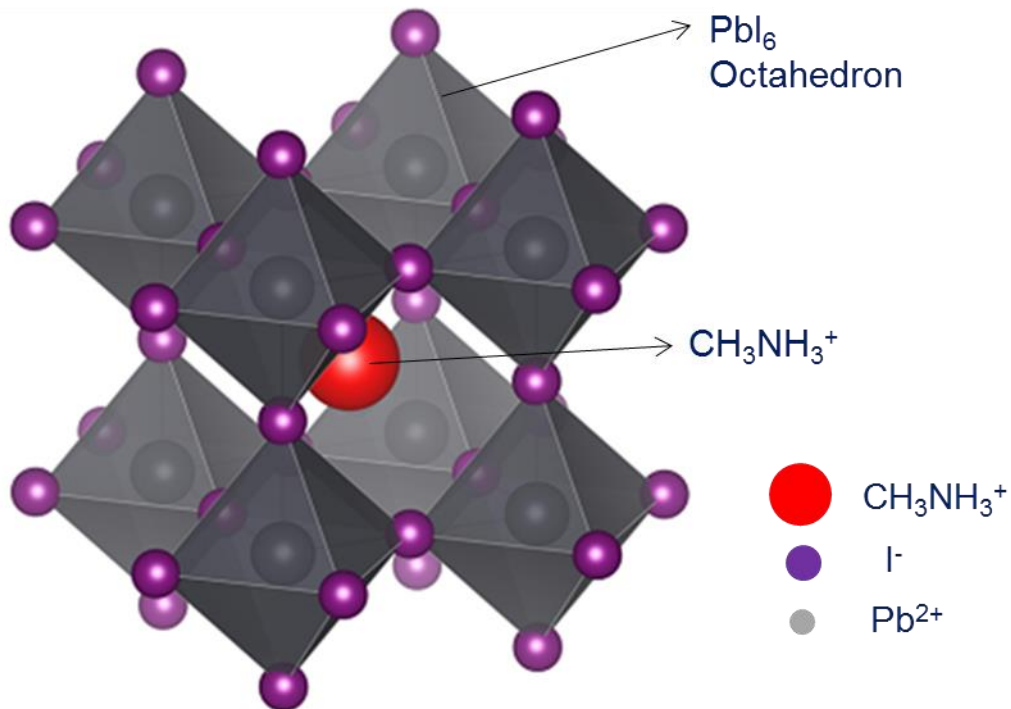


Figure 1: Structure of hybrid AMX_3 perovskite crystals^[8]

The most used perovskite material possesses relatively low (<50 meV) excitonic binding energy due to high dielectric constants up to 30 and a high electron mobility of around $66 \text{ cm}^2\text{V}^{-1}\text{s}^{-1}$ reported by Stoumpos et al. Because of its high carrier mobility, the most common perovskite material, methylammonium lead iodide (MAPbI₃ or CH₃NH₃PbI₃) was first studied as an active layer in field effect transistor. Also, the band gap energy of 1.5 eV is suitable to harvest sun light spectrum. Since Miyasaka et al fabricated very first CH₃NH₃PbX₃ based perovskite solar cell in 2009 with X = I, Br and yielded considerable efficiency of 3.8 % (X=I) and 3.1% (X=Br) respectively, a tremendous amount of work has been carried out to investigate perovskite solar cells and in about 5 years, the energy conversion efficiencies have recently reached over 20% [9].

1.2 Structure and Charge Transport Layers in Perovskite Solar Cells

There are mainly three kinds of well documented device architectures: mesoporous, regular planar and inverted planar structures as shown in fig. 2.

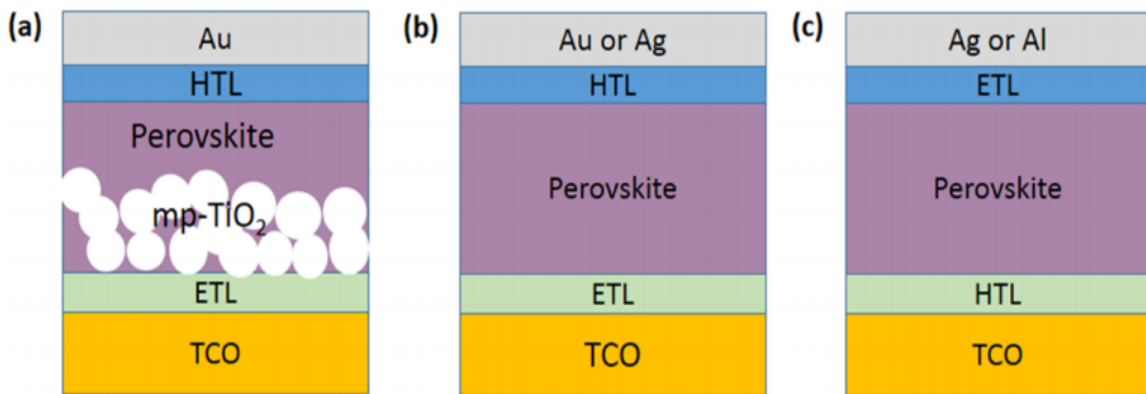


Figure 2: Three typical device structures of perovskite solar cells: (a) mesoporous, (b) regular (n-i-p) planar structure, and (c) inverted (p-i-n) planar structure [10]

Hybrid perovskite solar cell mechanism was first observed in DSSCs with mesoporous titanium oxide (TiO_2) structure and since then researchers have heavily studied this structure. Initial study in the perovskite solar cells using mesoporous structures faced challenges with film uniformity and device stability due to poor integration of perovskite precursor in the liquid electrolytes. Later the liquid electrolyte was replaced by Spiro-OMeTAD as the hole transport layer (HTL) and garnered ~10% power-conversion efficiency. In the recent years, mesoporous structures have achieved efficiencies close to 20% by optimizing the mesoporous- TiO_2 layer thickness and replacing MAPbI_3 with a smaller band gap material, formamidinium lead iodide (FAPbI_3). However, high temperature annealing is usually necessary to produce a TiO_2 layer with good crystallinity, which requires high temperature treatment thereby long processing time and relatively high cost. Although regular planar structures have reached higher efficiencies, hysteresis is a major problem when the sweep polarity is switched.

Inverted planar perovskite structure doesn't have any mesoporous scaffold layers. These structures usually use organic transport layer, poly(3,4-ethylenedioxythiophene) polystyrene sulfonate (PEDOT: PSS) or transition metal oxides such as NiO_x , MoO_3 , V_2O_5 and WO_3 as the HTL and fullerene derivative Phenyl-C61-butyric acid methyl ester (PCBM) as the electron transport layer (ETL). Inverted planar structures have considerably lower hysteresis compared to the regular structures. Although, the root cause of reduced hysteresis in inverted structure is still under study but the absence of meso- TiO_2 layer is believed to be the reason. Other attractive advantages of inverted planar structures over the regular structure include ease of fabrication and cost effectiveness. Due to the inclusion of high processing temperatures of the oxides based transport layers,

inverted planar structures without these oxide layers are preferred. In this dissertation, inverted planar structures with organic charge transport layers are used as a platform for device performance study.

In perovskite solar cells with any device architectures, perovskite active layer is always sandwiched in two charge transport layers: ETL and HTL. In terms of material types, these two charge transport layers can be either organic or metal oxide. The commonly used organic hole transport layers include poly(3,4-ethylenedioxythiophene) polystyrene sulphonate (PEDOT: PSS), 2,2',7,7'-tetrakis(N,N-pdimethoxyphenylamino)-9,9'-spirobifluorene (spiro-OMeTAD), poly[bis(4-phenyl)(2,4,6-trimethylphenyl)amine] (PTAA) and poly(3-hexylthiophene-2,5-diyl) (P3HT) ^[11–14]. PEDOT: PSS is a popular choice due to its ease in solution processing, high stable work function and due to its improved ohmic contact with active layer, which enhances hole collection and improves PCE. However, the acidic and hygroscopic nature of PEDOT: PSS may lead to corrosion of indium tin oxide (ITO) layer and degrade the perovskite absorber layer by leaking moisture and oxygen through pin holes^[15–20]. To address the degradation and stability issue caused by PEDOT: PSS, inorganic metal oxides such as NiO_x are used as p-type hole transport layer^[21–24]. These metal oxides possess higher carrier mobilities and are more stable compared to their organic counter parts. However, these oxide layers require high temperature processing, excess of 300°C, making its application difficult in roll-to-roll printing of flexible solar cells.

The most commonly used electron selective layers in perovskite solar cells are Titanium dioxide (TiO₂) and Zinc oxide (ZnO) because of their large band gaps and high electron mobilities. Inorganic electron transport materials such as Aluminum oxide

(Al₂O₃), Cesium Carbonate (Cs₂CO₃) and Lithium fluoride (LiF) have also been reported to be used as ETL and improve the device performance.

By employing different perovskite processing methods and alternate fullerene derivatives substantial research has been conducted in the inverted perovskite structures as summarized in the table 1.^[10]

Table 1: Several representative devices performances of inverted planar structured perovskite solar cells

perovskite processing	HTL	ETL	V _{oc} (V)	J _{sc} (mA/cm ²)	FF (%)	PCE (%)	stability
one-step	PEDOT:PSS	PC ₆₁ BM/BCP	0.60	10.32	63	3.9	
two-step	PEDOT:PSS	PC ₆₁ BM	0.91	10.8	76	7.4	
one-step (Cl)	PEDOT:PSS	PC ₆₁ BM	0.87	18.5	72	11.5	
one-step (Cl)	PEDOT:PSS	PC ₆₁ BM/TiO _x	0.94	15.8	66	9.8	
solvent engineering	PEDOT:PSS	PC ₆₁ BM/LiF	0.87	20.7	78.3	14.1	
one-step (moisture, Cl)	PEDOT:PSS	PC ₆₁ BM/PFN	1.05	20.3	80.2	17.1	
one-step (hot-casting, Cl)	PEDOT:PSS	PCBM	0.94	22.4	83	17.4	
one-step (HI additive)	PEDOT:PSS	PC ₆₁ BM	1.1	20.9	79	18.2	
coevaporation	PEDOT:PSS/Poly-TPD	PC ₆₁ BM	1.05	16.12	67	12.04	
coevaporation	PEDOT:PSS/PCDTBT	PC ₆₁ BM/LiF	1.05	21.9	72	16.5	
two-step spin-coating	PTAA	PCBM/C60/BCP	1.07	22.0	76.8	18.1	
one-step solvent	PEDOT:PSS	C ₆₀	0.92	21.07	80	15.44	
one-step (Cl)	PEDOT:PSS	PC ₆₁ BM/ZnO	0.97	20.5	80.1	15.9	140 h
one-step (Cl)	PEDOT:PSS	PC ₆₁ BM/ZnO	1.02	22.0	74.2	16.8	60 days
one-step	NiO _x	PC ₆₁ BM/BCP	0.92	12.43	68	7.8	
one-step	NiO _x :Cu	PC ₆₁ BM/C ₆₀ -bis surfactant	1.11	19.01	73	15.4	244 h
solvent engineering	NiO _x	PC ₆₁ BM/LiF	1.06	20.2	81.3	17.3	
two-step	NiO _x	ZnO	1.01	21.0	76	16.1	>60 days

1.3 Stability of Perovskite Solar Cells

Although much of the focus have been on improving the efficiency of the organic-halide perovskite solar cells, degradation of these cells has been much of a concern. For perovskite, solar cells to be commercially available as a viable replacement for the existing photovoltaic technologies, it must overcome the problem of stability and degradation. One of the main issues causing instability is when perovskite layers are subjected to moisture and oxygen. The hydrophilic and volatile nature of methylammonium lead iodide makes it prone to degradation through humidity and heat. The presence of moisture and oxygen results in non-reversible degradation process in

Methylammonium (MAI) based perovskite solar cells because MAI hydrolyzes in presence of moisture and oxygen. [25] Gratzel et al in their work suggested that it is important to attain extremely high humidity of <1% to power conversion efficiencies over 15%. Guangda Niu et al also found a similar trend and emphasized on the humidity[27]. Niu et al. have reported a detailed study of decomposition in perovskite absorber layer identifying ultraviolet (UV) light, solution processing techniques and thermal effects along with moisture and oxygen as the key factors causing degradation.[27]

From the perovskite crystal structure, it can be inferred that methylammonium cation via hydrogen bonds is weakly bonded with lead and halide ions. This weak bonding can result in breaking of bonds with exposure to water molecules. The stability problem in the perovskite absorber layer can be overcome by modifying the elemental composition of the perovskite absorber material. Perovskite absorber layer stability can also be controlled by adding functional molecules or polymer additives to absorber layer material. These nanometer-sized polymer additives help crosslinking the neighboring perovskite grains and wraps the crystal surface making absorber layer less susceptible to moisture and oxygen.

Plenty of extensive studies have been carried on to address the stability of the whole device and the absorber layer itself. Addition of polymer additives to perovskite absorber layer has shown to improve the crystallinity and increase the device stability. Halogen additives such HI, alkyl halides, phosphonium halides, NH_4Cl , CaCl_2 have also been reported to enhance the device performance[28–32]. Polyethyleneimine (PEI) has shown to control the crystal-growth of the perovskite film. Addition of Polyethylene glycol (PEG) additive to perovskite precursor have shown to improve the morphology of

the perovskite film^[33]. Stability of perovskite absorber layer have shown to be improved with bifunctional 4-ABPA ammonium cation^[34].

1.4 Working Principle of Perovskite Solar Cells and Device Characterization

As stated before, in this study inverted structure with organic charge transport layer is utilized because of easy fabrication and avoiding high-temperature processing of metal oxides. The inverted architecture of perovskite solar cells is shown in Figure. 3(a). It consists of ITO anode, PEDOT: PSS hole transport layer, perovskite light absorbing layer, PCBM electron transport layer, and aluminum cathode.

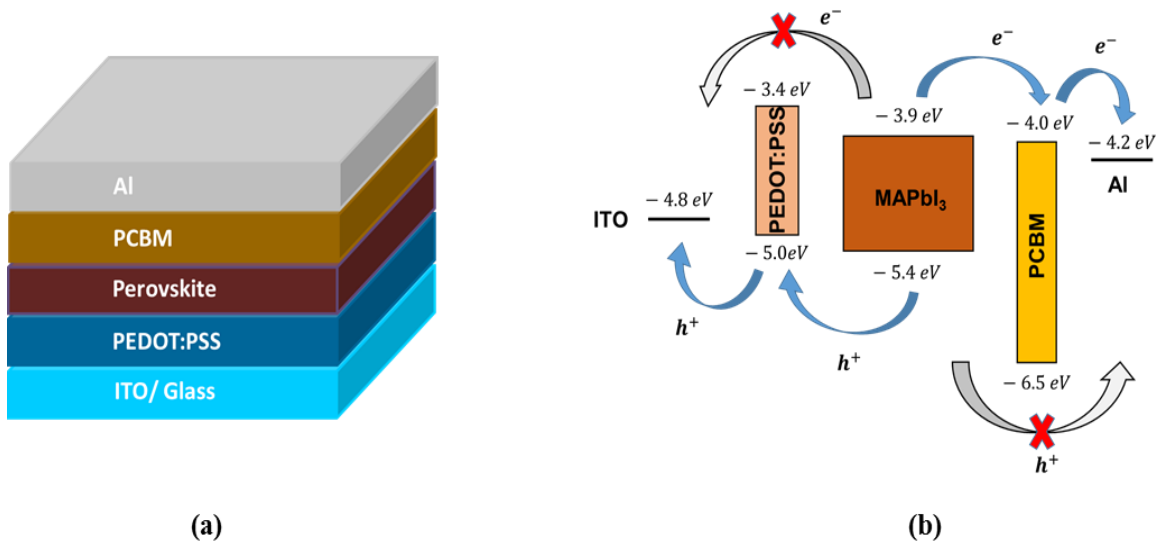


Figure 3: (a) Schematic of inverted perovskite solar cell structure used in the project, (b) energy band diagram showing charge carrier transport and collection.

In a typical photovoltaic device, photo-excited charge carrier undergoes three major steps: generation of charge carriers, charge transport and collection at the electrodes. First, electrons and holes are generated when a photon is absorbed by the perovskite absorber layer. Bandgap of the perovskite absorber layer determines the number of photons that can be absorbed. Photons whose energy is higher than the bandgap of the absorber layer are absorbed and broken down to free electron and hole charge carriers, while incident photons whose energy is lower than the bandgap will go through without absorption. Low bandgap materials ensure more absorption of photons; however, narrow band gaps can also harm the device by compromising the photovoltage.

Photo generated charges are transported to the corresponding electrodes through electron and hole transport layers. Generally, larger diffusion lengths in active layer are beneficial in transport of charges as the charges can reach the buffer layer interfaces before being recombined. In the charge collection process, electrons are collected at the metal cathode (Al, Ag) through electron transport layer and holes are collected at the ITO anode through hole transport layer. These charge selective electron and hole transport layers play a crucial role in the charge transport and collection process. These layers help in reducing the energy barrier between perovskite absorber layer and the respective electrodes thereby minimizing the interfacial recombination of charges.

Figure. 3 (b) shows energy band diagram of inverted perovskite solar cells with ITO/PEDOT: PSS/Perovskite/PCBM/Al structure. Energy band diagram is an important tool to show charge transport and collection. As the sunlight shines on the perovskite solar cells, the photons with energy greater than band gap of perovskite semiconductor will be absorbed and generate electron and holes as free charge carriers. Electrons in the

conduction band like balls move from perovskite active layer through PCBM electron transport layer and are collected at Al cathode. Meanwhile, holes in the valence band like bubbles transport from perovskite layer to PEDOT: PSS hole transport layer and are collected at ITO anode. From the energy band diagram, it can be noticed that PCBM ETL layer also serves as hole blocking layer from hole collection at Al cathode, and PEDOT HTL acts as electron blocking layer from electron transport and collection at ITO anode. Therefore, charge transport layers facilitate collection of respective charges to the corresponding electrodes and block the undesired charges. The accumulation of positively charged holes at ITO anode and negatively charged electrons at Al cathode creates electric field between electrodes thereby generating electricity.

The power-conversion efficiency (PCE) can be characterized by current versus voltage measurement. Since current depends on device area, current density is the parameter to characterize the performance of solar cells. Figure 2 shows the schematic of current density versus voltage (J-V) curve. PCE is the ratio of maximum electrical power output to the incident light power (Equation 1). Another parameter called fill factor (FF) is defined as the ratio of maximum output power to the product of short-circuit current (J_{sc}) and open-circuit voltage (V_{oc}), which is indicated by the shape of the J-V curve, the squarer the J-V curve, higher the FF. Short-circuit current is the current when the solar cell is short-circuited, the voltage across the cell is zero. Open-circuit voltage is the maximum voltage through solar cell when the current is set to zero. Based on Equation 3, the efficiency of a solar cell is determined by short-circuit current density, open-circuit voltage and fill factor (FF). Power conversion efficiency of a solar cell can be greatly improved by increasing these parameters.

$$\eta = \frac{J_m \cdot V_m}{P_{in}} \dots \dots \dots (1)$$

$$FF = \frac{J_m \cdot V_m}{J_{sc} \cdot V_{oc}} \dots \dots \dots (2)$$

$$\eta = \frac{J_{sc} \cdot V_{oc} \cdot FF}{P_{in}} \dots \dots \dots (3)$$

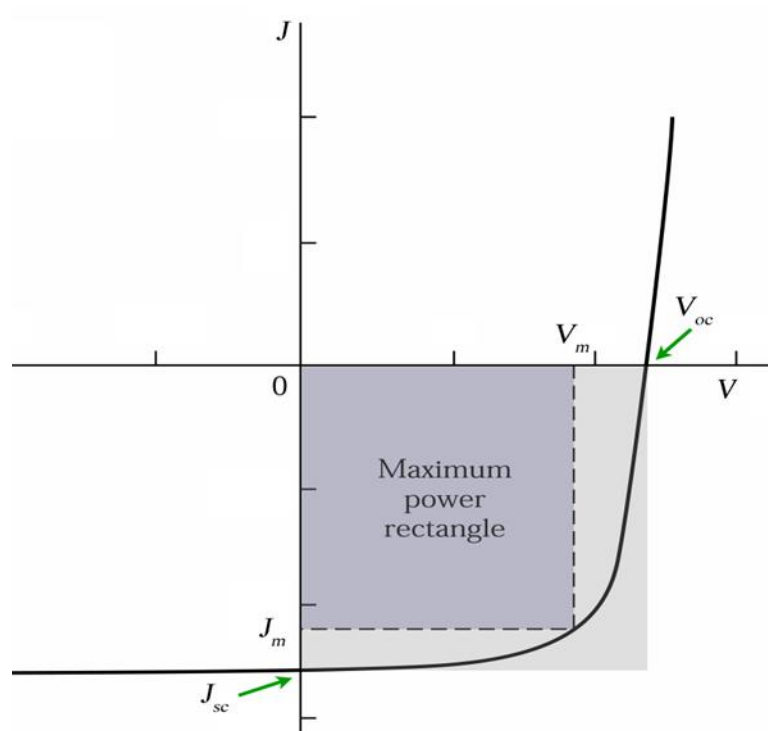


Figure 4: J-V curve of a solar cell

CHAPTER 2. SIMULATION STUDY OF PEROVSKITE SOLAR CELLS

2.1 Introduction

Semiconductor device simulator is a powerful tool to get physical insight and guide experiments. Here a commercial software, semiconducting emissive thin film optics simulator (SETFOS), is employed to study opto-electronic properties of multi-layer organic and perovskite solar cells. By varying input parameters, such as layer thickness, mobility, recombination, the device performances can be simulated. Based on physical insight from the device simulation and parameter optimization, experiments can be guided to attain high performance solar cells.

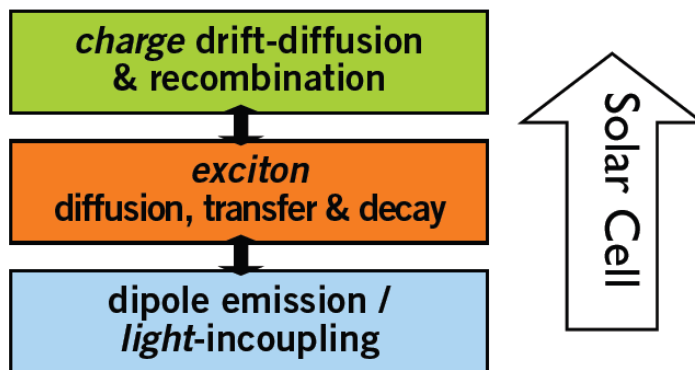


Figure 5: Simulation workflow of SETFOS for photovoltaic devices

Fig. 5 shows the workflow of SETFOS simulation for organic and perovskite solar cells. SETFOS first calculates the reflectance (R) and transmittance (T) as a function of wavelength. The absorbance (A) is then determined based on the conservation of energy

$A = 1 - (R+T)$. The absorption profile of every individual layer is derived by using the refractive index (n) and extinction co-efficient (k) values.

When light passes through a medium, some part of it will always be attenuated. This can be conveniently considered by defining a complex refractive index.

$$n = n + ik$$

Then the absorption coefficient can be expressed in terms of extinction coefficient as:

$$\alpha = \frac{(4\pi k)}{\lambda}$$

And Transmission

T is given by

$$T = \exp(-\alpha d)$$

Where ' α ' is the absorption coefficient and ' d ' is the thickness. In the above equation scattering losses are neglected and the fraction of radiation lost ($1-T$) is attributed entirely to absorption.

$$\begin{aligned} A &= 1 - T \\ &= 1 - \exp(-\alpha d) \end{aligned}$$

Refractive index and extinction coefficient values extracted from literature or experiments were plugged in SETFOS to obtain absorbance for the perovskite absorber layer.

After light absorption, electron and hole pairs (excitons) are generated. After dissociation, free electrons and holes are created. To calculate the charge carrier transport as drift and diffusion, the semiconductor continuity equations are used.

$$\frac{dn}{dt} = \frac{\vec{v} \cdot \vec{J}_n}{q} - R - \frac{dn}{dt} + g_{opt_{np}} G_n$$

$$\frac{dp}{dt} = \frac{\vec{v} \cdot \vec{J}_p}{q} - R - \frac{dp}{dt} + g_{opt_{np}} G_p$$

Where n is the density of electrons, p is the density of holes, R is recombination, $\frac{dnt}{dt}$ and $\frac{dpt}{dt}$ denotes charge capture by traps and $gopt_{np}$ is the generation efficiency.

The simulation parameters used in this study are summarized in table below. Perovskite has good absorption and the optimum thickness selected for simulations was around 300nm. The highest occupied molecular orbital (HOMO) and lowest occupied molecular orbital (LUMO) of perovskite layer are 3.9 eV and 5.4 eV which constitutes to a favorable bandgap of 1.5 eV. Perovskites have high electron, $5 \text{ cm}^2\text{V}^{-1}\text{s}^{-1}$ and hole mobility, $5 \text{ cm}^2\text{V}^{-1}\text{s}^{-1}$

Table 2: Input parameters used for perovskite solar cell simulation

Parameter	Symbol	Value	Unit
Thickness (perovskite)	$Th_{\text{perovskite}}$	300	nm
LUMO (perovskite)	$LUMO_{\text{perovskite}}$	3.9	eV
HOMO (perovskite)	$HOMO_{\text{perovskite}}$	5.4	eV
Dielectric constant (perovskite)		10	-
Electron mobility	μ_n	5	$\text{cm}^2\text{V}^{-1}\text{s}^{-1}$
Hole mobility	μ_p	5	$\text{cm}^2\text{V}^{-1}\text{s}^{-1}$
Langevin recombination efficiency	η_R	0.08	1
Optical charge generation efficiency		1	1

2.2 Influence of Different PCBM and Cathode Materials on PCE

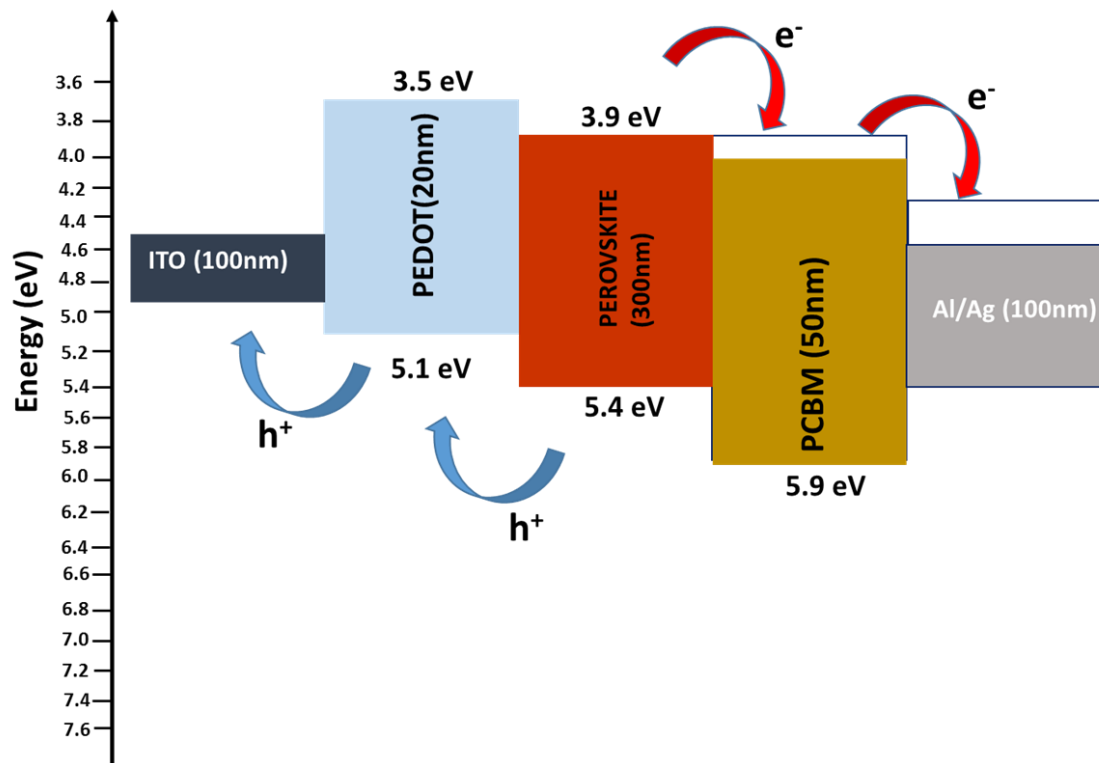


Figure 6: Energy band diagram of perovskite solar cells with inverted structure of ITO/PEDOT/Perovskite/PCBM/Cathode. ETL layer is either PC₆₁BM and PC₇₁BM with Al or Ag cathode.

In the inverted structure of ITO/PEDOT/Perovskite/PCBM/Cathode, PCBM serves as an electron transport layer to facilitate transport of electrons from perovskite absorber to Al/ Ag electrode. There exist two kind of PCBM: PC₆₁BM and PC₇₁BM with different LUMO energy levels. PC₆₁BM has LUMO energy level of 3.9 eV, the same as the perovskite semiconductor. PC₇₁BM has LUMO energy level of 4.1 eV, lower than the LUMO of perovskite, which will facilitate electron transport to cathode. As shown in the Table 3, with the same cathode, perovskite solar cells with PC₇₁BM as ETL always demonstrate better performance than those with PC₆₁BM. As for the cathode metal, typically used materials are low work function metal Al and Ag. Metal Al has work function of 4.26 eV, smaller than Ag work function of 4.6 eV, which means the Fermi

level of Ag is lower than Al. The large energy difference between LUMO of PC₇₁BM and Fermi level of Ag results in hindering efficient electron transport thereby lowering the PCE, which is indicated in Table 3. The optimum combination for energy level matching is with PC₇₁BM and Al electrode, attaining an efficiency of 13%, which is higher than the worst case of PC₆₁BM with Ag cathode (PCE = 7.9%).

Table 3: Device performance with PCBM ETL and Al/ Ag cathode

Fullerene and Electrode	V_{oc}	J_{sc}	FF	Efficiency
PC ₆₁ BM with Ag	0.669	22.660	0.5206	7.8925
PC ₆₁ BM with Al	0.748	22.146	0.659	10.9188
PC ₇₁ BM with Ag	0.755	22.668	0.6133	10.5007
PC₇₁BM with Al	0.714	22.160	0.8235	13.0313

2.3 Effect of P3HT Hole Mobility on Efficiency

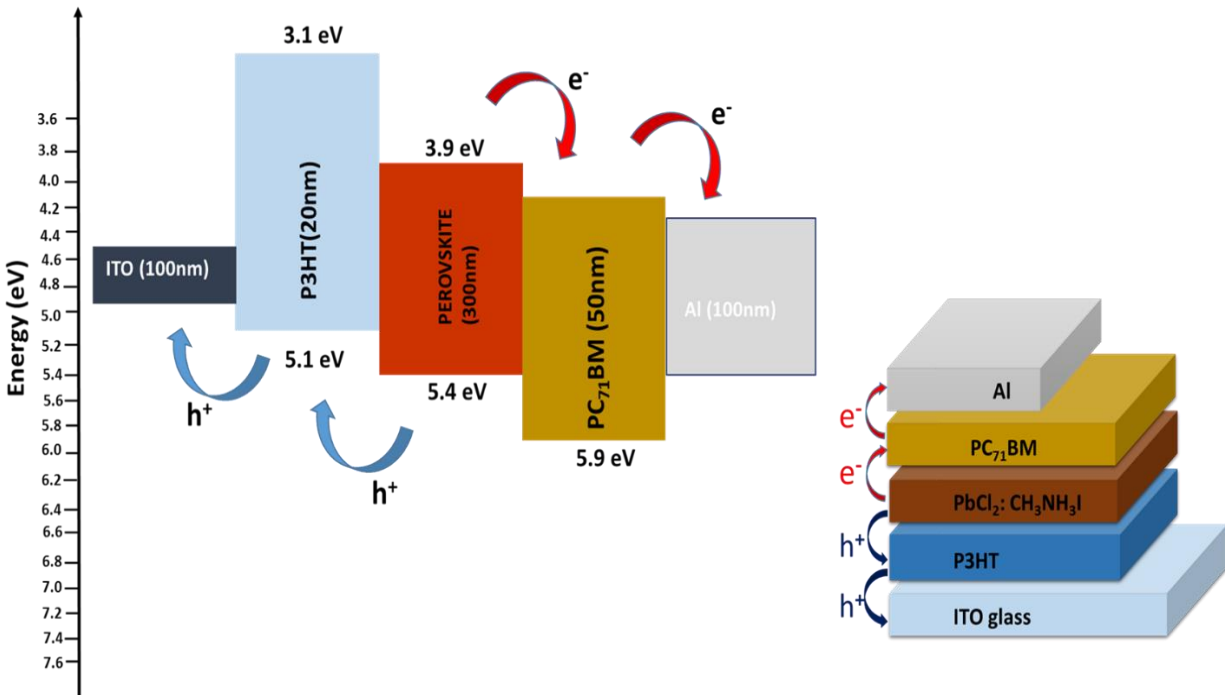


Figure 7: Energy band diagram with P3HT as HTL in inverted perovskite solar cells

Conventionally P3HT is used as a strong electron donor in organic solar cells. Recent research has demonstrated that P3HT can serve as a HTL in inverted perovskite solar cells to facilitate transport of holes from perovskite absorber layer to the holes collecting ITO electrode. Herein, the effect of P3HT hole mobility on the overall device performance was studied. From the band diagram in fig. 7, HOMO energy level of P3HT matches well with the HOMO of perovskite active layer. Hole mobility is responsible for transport of holes via P3HT hole transport layer to the ITO electrode. The simulation results in Figure 8 show that as the hole mobility of P3HT layer increases, the open circuit voltage and fill factor increases accordingly. As the hole mobility in P3HT increases, less photo-carriers are accumulated inside the bulk thereby reducing the charge carrier

recombination. As a result, the power conversion efficiency increases as hole mobility in P3HT increases.

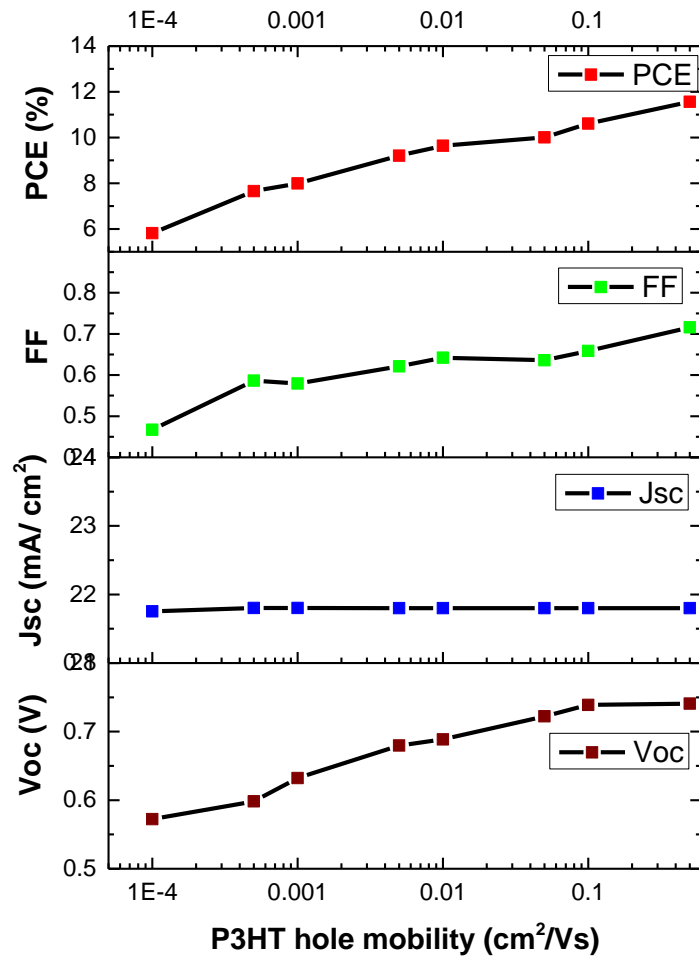


Figure 8: Effect of P3HT hole mobility on efficiency

2.4 PCE versus ITO Work Function

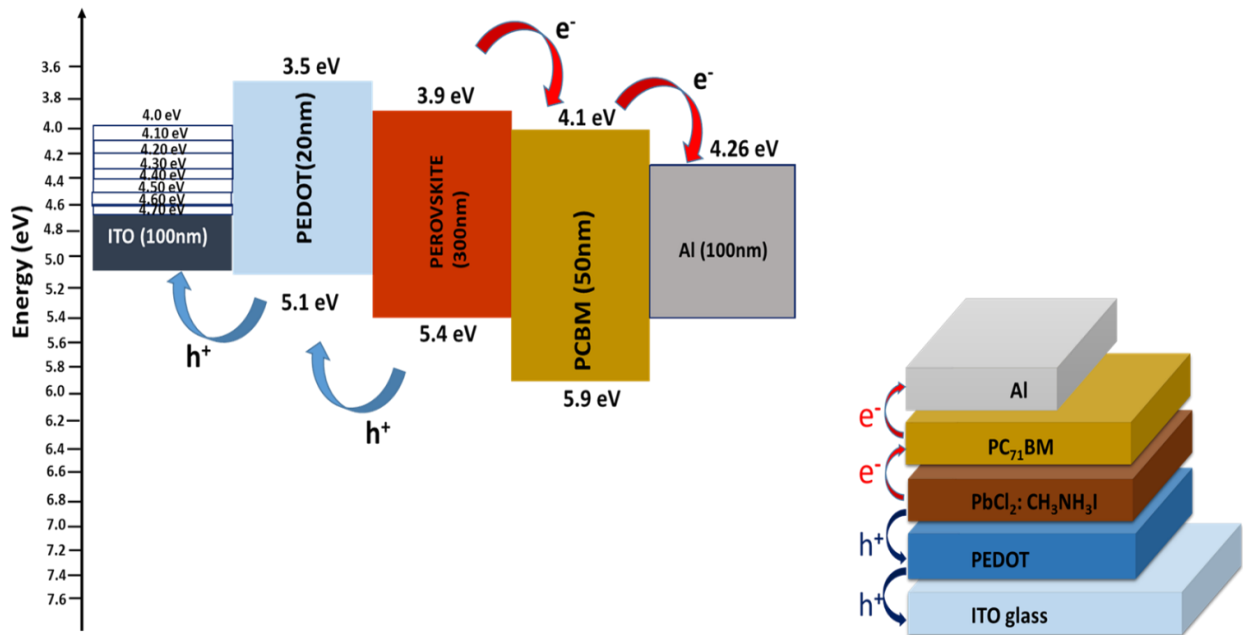


Figure 9: Energy band diagram with PEDOT HTL and PCBM ETL

For the conventional inverted perovskite solar cells with ITO/PEDOT/Perovskite/PCBM/Al structure, the effect of ITO work function change on the device performance was also investigated in this study. Fig. 9 shows the energy band diagram with ITO work function variation from 4.0 eV to 4.7 eV. Upon light absorption by perovskite active layer, the generated electrons move through PCBM and are collected at Al cathode, while holes transport through PEDOT layer for collection at ITO anode. Both electrons and hole are not able to transport to the opposite directions because PCBM ETL also serves as hole blocking layer and PEDOT HTL acts as electron blocking layer. As demonstrated before for electron transport from PCBM to Al cathode, the appropriate energy difference between LUMO of PCBM and Al Fermi level is critical. Herein, the energy difference between HOMO of PEDOT and Fermi level of ITO was also studied.

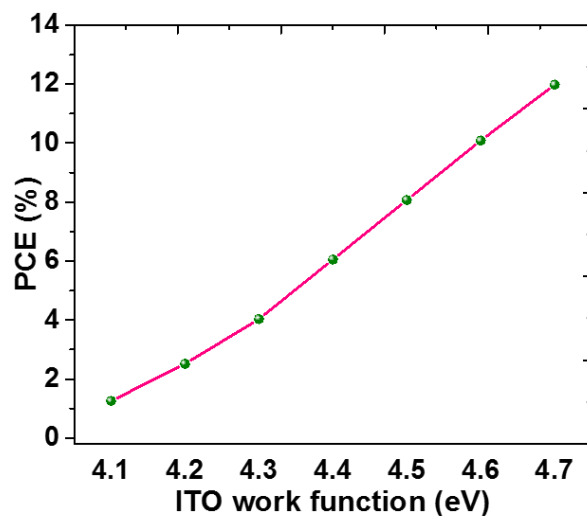


Figure 10: Efficiency vs ITO work function

Fig. 10 shows the effect of ITO work function modification on overall PCE of the device. As increase in ITO work function lowers the Fermi level, facilitating hole injection from PEDOT HTL to ITO anode. The closer the work function of ITO is increased to the HOMO of PEDOT, the more convenient for holes transport and being collected at ITO anode, leading to overall enhancement of PCE.

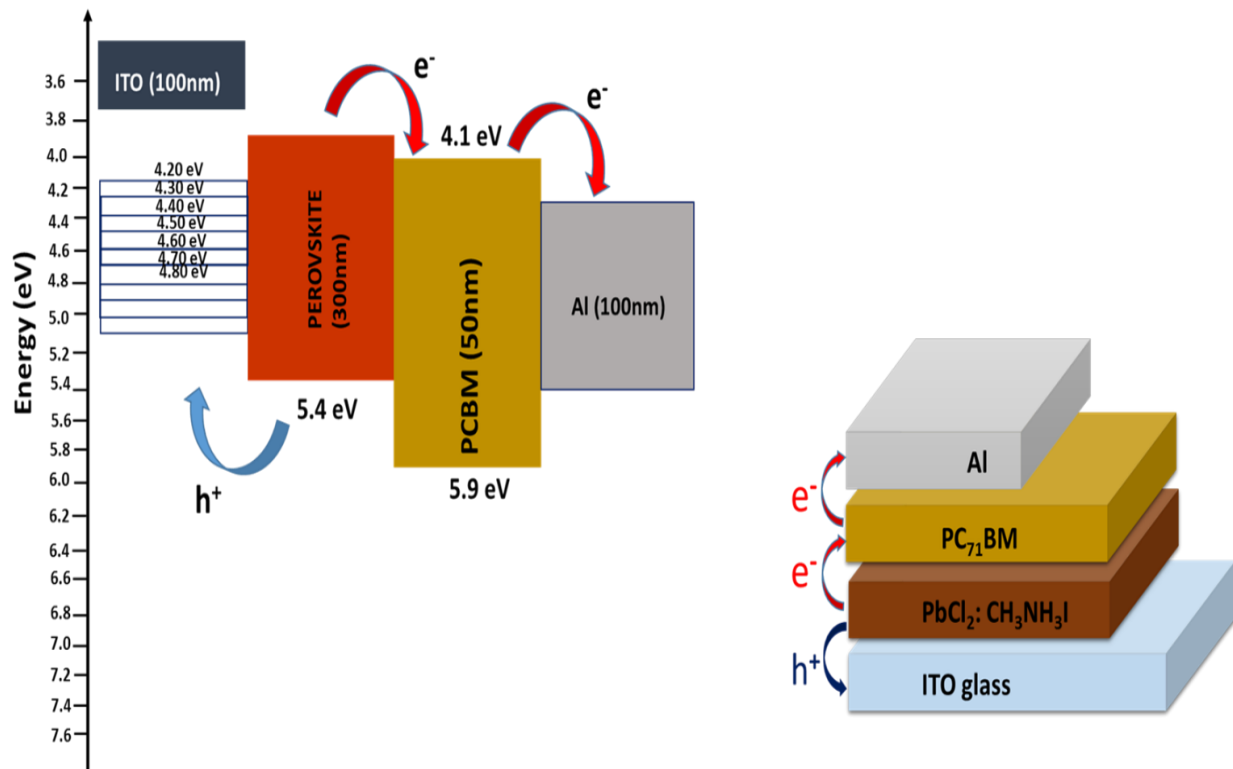


Figure 11: Energy band diagram without PEDOT hole transport layer

Although PEDOT is a conventional choice serving as HTL in inverted perovskite solar cells, the hygroscopic and acidic nature of PEDOT can corrode ITO layer and degrade the perovskite active layer thereby causing the solar cell degradation. Fig. 11 shows the energy band diagram of typical inverted perovskite solar cells without PEDOT HTL layer. The effect of ITO work function modification without the PEDOT hole transport layer between perovskite absorber layer and ITO electrode was also investigated. As shown in fig. 12, without PEDOT hole transport layer, the correlation between power conversion efficiency and ITO work function follows similar trend, i.e. as ITO work function increases, PCE is improved. However, without PEDOT hole transport layer, the overall power conversion efficiency is lower compared to case with PEDOT at same ITO work function. As a hole transport layer, PEDOT can smooth the energy step

between perovskite and ITO, creating appropriate energy difference for hole transport from perovskite to ITO.

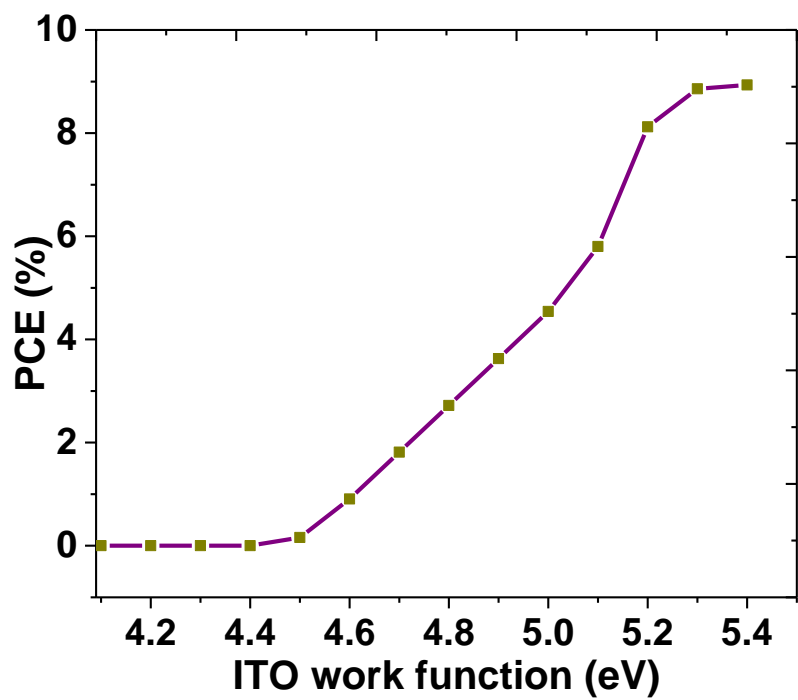


Figure 12: Efficiency vs ITO work function

CHAPTER 3. SIMULATION STUDY OF ORGANIC POLYMER SOLAR CELLS

3.1 Introduction

Organic photovoltaic (OPV) technology has received great attention in the past decade because of easy fabrication and cost effective over a large area, and the power-conversion efficiency has improved from about 1% in to more than 10%, which is from organic bulk heterojunction solar cells^[35-41]. Compared to the inorganic semiconductors which have low exciton binding energy due to high di-electric constant, organic semiconductors require substantial energy to dissociate the excitons into free electrons and holes because of their lower di-electric constants and strong Coulomb interaction^[38,42]. Also, organic semiconductors have low charge transport mobilities. Charge transport between molecules is by hopping instead of moving in the energy band due to weak van der waals interaction in organic semiconductors. Although afore mentioned properties, organic semiconductors have demonstrated high absorption coefficients, requiring very thin absorber layer to harvest sunlight spectrum^[43], and the solution processable capability enables organic solar cells to be manufactured using low-cost roll-to-roll printing. Researchers throughout the world have made every effort in improvement of the efficiency by synthesis of new novel materials, understanding the device mechanism, engineering new device architectures, improving the charge carrier transport by designing new pathways^[40].

The schematic in fig. 13 shows the basics steps involved in light harvesting of the organic molecules, exciton generation/diffusion/separation, charge transport and collection at electrodes. During the energy conversion process, both excitons and free charge carriers can be recombined thereby the absorbed photons are wasted.

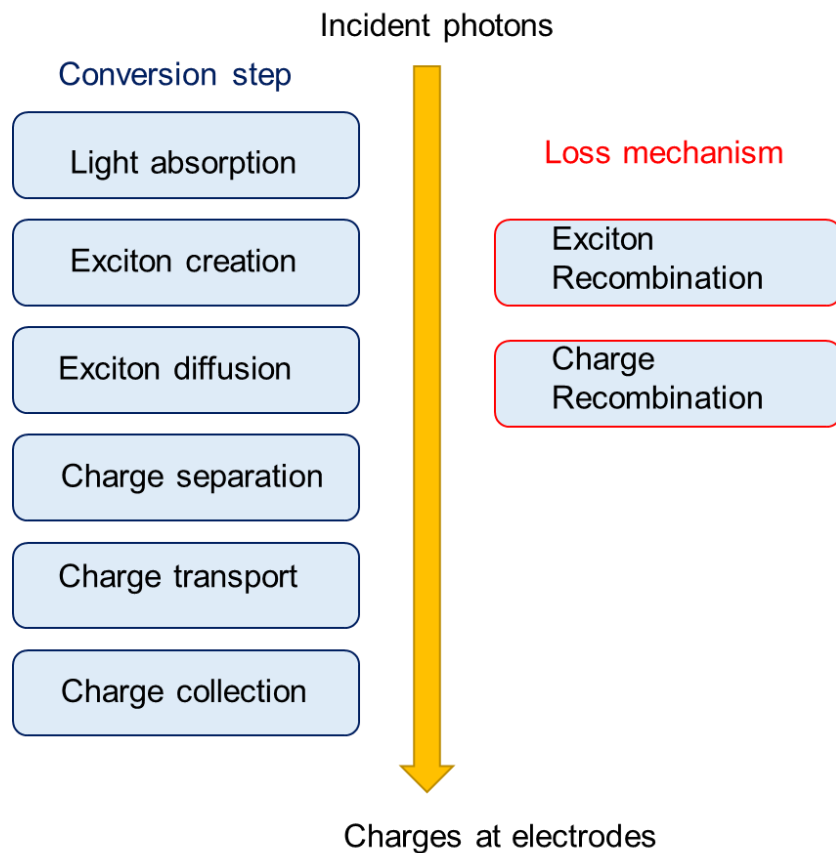


Figure 13: Schematic flow chart showing the steps converting sunlight to electricity in organic photovoltaics.

Currently bulk heterojunction PV cells based on polymer-fullerene derivatives (electron donor-acceptor) are the most successful organic solar cells. A typical BHJ solar cell configuration is shown in fig. 14, in which the active layer consisting of the donor and acceptor blend is sandwiched between a transparent anode on glass and metal

cathode. The sun light is usually absorbed in the conjugated polymer layer (electron-donating semiconductor), and strongly Coulomb-bound electron-hole pairs known as excitons are generated inside the donor polymer. Before dissociation, photogenerated excitons must diffuse towards the fullerene derivative (electron acceptor) and reach the donor-acceptor interface first. Because of the energy offset between electron donor and acceptor materials at the interface (heterojunction), excitons are separated with free electrons moving into low-energy states in acceptor and holes transporting in the donor material. Finally, electricity is generated when electrons are collected at top metal cathode and holes reach the transparent conducting oxide (TCO) anode. The formation of heterojunction structure in organic solar cell development is a quantum leap for significant increase of power-conversion efficiency^[39,40].

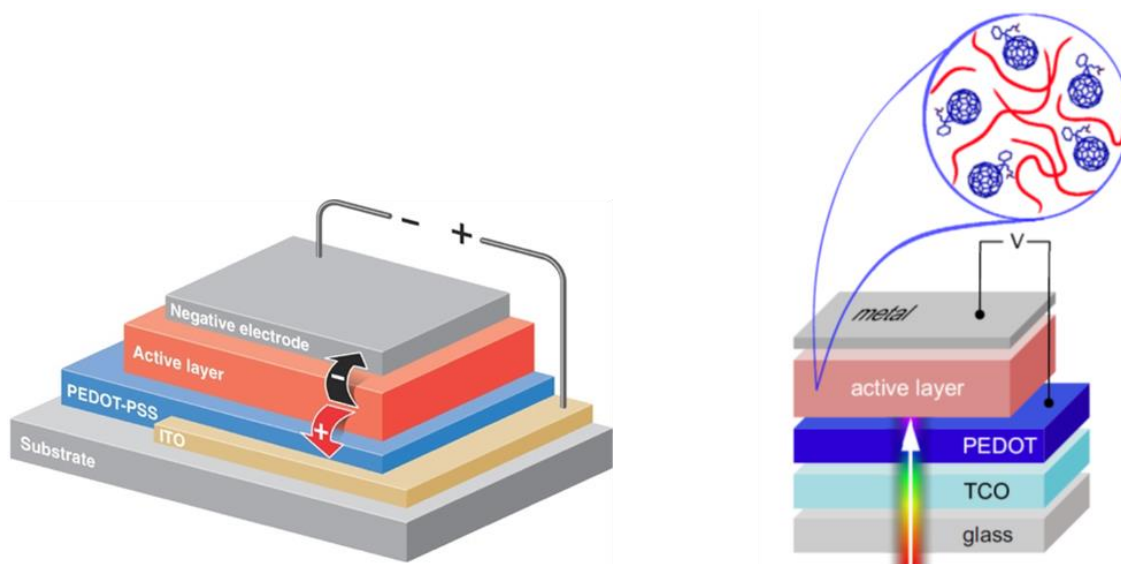


Figure 14: Schematic of conventional (regular) polymer-fullerene bulk heterojunction solar cells. A blend of conjugated polymer with a fullerene derivative serves as active layer. A transparent conductive oxide (TCO) such as ITO acts anode, and a top metal electrode^{[44][45]}

Although conventional (regular) organic solar cells have resulted in high efficiencies, there are some underlying issues which are hindering the further improvement of the OSCs. In the conventional organic solar cell structure as shown in fig. 14, ITO is used as the efficient hole collecting electrode (anode) and a layer of PEDOT: PSS is used as a hole transporting layer. The strong acidic nature of PEDOT: PSS results in the corrosion of ITO/ PEDOT interface over the period of time. The degradation of ITO/ PEDOT interface quality inevitable reduces the solar cell performance. Conventional solar cell structure also uses low-work function metal, aluminum (Al) as top electron collecting layer (cathode) which is widely regarded as air-sensitive in nature.

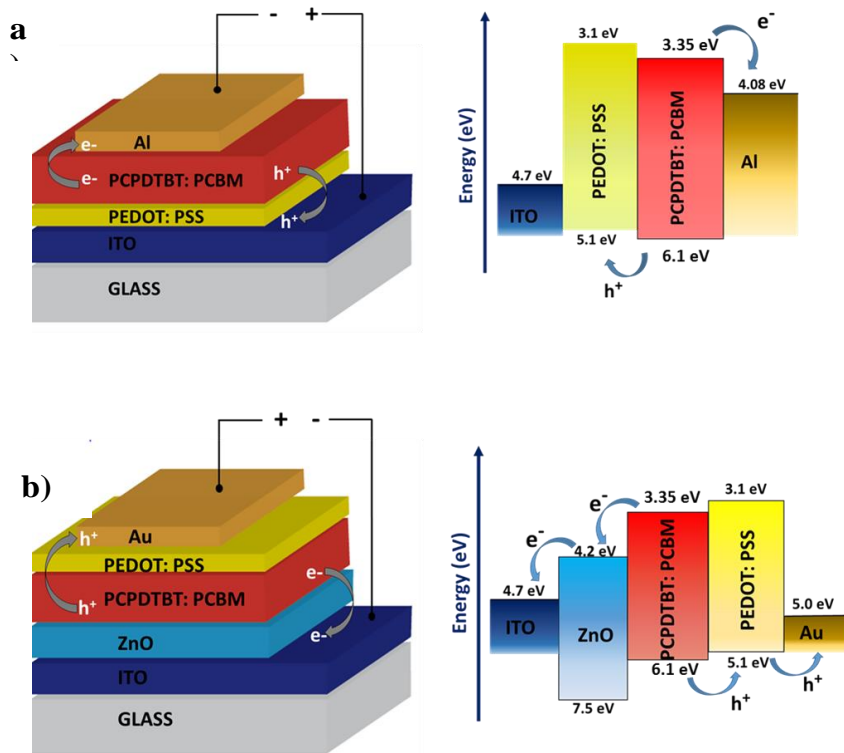


Figure 15: Schematic of solar cell configuration for a) Regular structure: ITO (anode) glass/ PEDOT: PSS/ PCPDTBT: PC70BM/ Al (cathode) b) Inverted structure: ITO (cathode) glass/ ZnO/ PCPDTBT: PC70BM/ PEDOT: PSS/ Au (anode)

Air-sensitive issue of Al electrode makes a way for the diffusion of oxygen and moisture in the underlying active layer through pinholes and grain boundaries, damaging the device stability.

To address stability issue in OSCs with regular structure, inverted OSC architecture was developed as shown in fig. 15(b). Instead of PEDOT hole transport layer on the top of ITO electrode, electron collecting buffer layer, such as ZnO or TiO₂, is deposited on the ITO surface. After spin-coating of active layer, metal oxides such as MoO₃ or V₂O₅ is deposited on the top of it as hole transport layer followed by the thermal evaporation of air-stable and high work-function metals such as gold (Au) and silver (Ag) as anode. Therefore, in the inverted architecture, the polarity of charge transport and collection is reversed and bottom contact ITO serves as an electron collecting electrode (cathode). In addition, the use of ZnO/ TiO₂ electron collecting buffer layers to replace acidic PEDOT: PSS and replacement of air-sensitive top electrode with a stable high work-function electrode results in an improved device stability.

3.2 Inverted Device Structure and Materials in Simulation

An inverted solar cell structure has been shown to be a promising solution to increase the air stability of organic bulk-heterojunction photovoltaic cells while preserving their solution processibility and ability to be fabricated on a variety of flexible substrates. In this structure, conducting polymer PEDOT:PPS serves not only as a hole transport layer, but also as a protecting layer to block the diffusion of oxygen into the active layer. Air stability is further increased by replacing low work function Aluminum with a higher work function, higher stability metal on top of PEDOT:PPS as the anode. In

this study, low band gap polymer Poly[2,6-(4,4-bis-(2-ethylhexyl)-4H-cyclopenta [2,1-b;3,4-b']dithiophene)-alt-4,7(2,1,3-benzothiadiazole)] (PCPDTBT), was used as donor polymer in the inverted solar cell architecture: ITO/ETL/PCPDTBT: PCBM/ PEDOT: PSS/ Au as shown in Figure x. PCPDTBT and PC₇₀BM were chosen as donor and acceptor molecules because of their broad-spectrum absorption due to the low bandgap nature of the PCPDTBT polymer (~1.46eV). The chemical structure of PCPDTBT and PC₇₀BM molecules are shown in Figure x. The effects of PCPDTBT: PCBM active layer thickness, charge carrier mobility, the Langevin recombination rate, and electron transport layer selection on power-conversion efficiency (PCE) were systematically investigated.

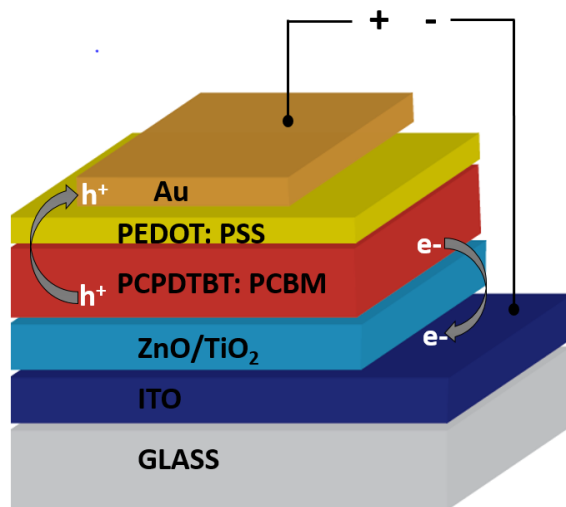


Figure 16: Inverted organic solar cell configuration: ITO (cathode) glass/ ZnO/PCPDTBT: PCBM/ PEDOT: PSS/Au (anode)

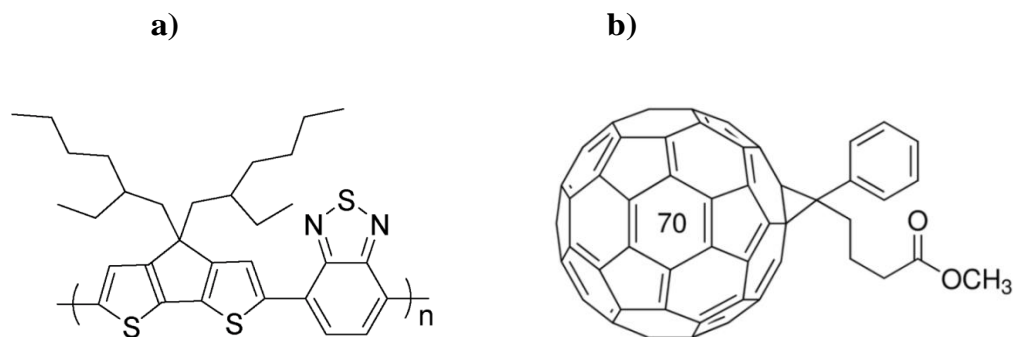


Figure 17: Chemical structure of a) PCPDTBT polymer b) PC₇₀BM [46]

3.3 Optimization of Active Layer

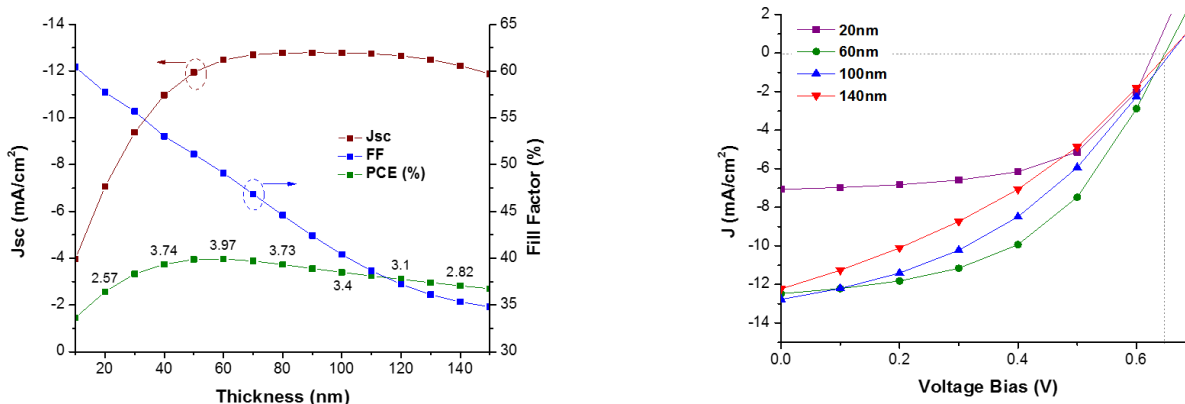


Figure 18: a) Variation of efficiency, short-circuit current density and fill factor with active layer thickness b) Simulated J-V characteristics as a function of active layer thickness.

Since active layer thickness plays critical role in performance of organic bulk heterojunction solar cells, it has always been the first device parameter to be optimized. The optimized active layer thickness can balance the light absorption and charge carrier recombination, reaching the best performance with the given material system. In this study, the active layer thickness was also first optimized based on a given electron mobility of $6E-3 \text{ cm}^2/\text{Vs}$, a hole mobility of $1E-4 \text{ cm}^2/\text{Vs}$, and a Langevin recombination

rate of 0.5. Langevin recombination rate is a parameter to characterize the recombination of electrons and holes during transportation in the device. As seen from fig. 18a, PCE reaches a maximum value of 3.97 with an active layer thickness of 60nm, where light absorption and recombination are anticipated to be well balanced. The efficiencies at active layer thickness smaller and larger than 60nm are always lower than this peak efficiency. This peak efficiency can be explained by the variation of short-circuit current density and fill factor as a function of active layer thickness. As the active layer thickness increase, more sun light can be absorbed, resulting in the increase of J_{sc} . On the other hand, the increase of active layer thickness cause more recombination of electrons and holes because these charge carriers have to transport longer distance to reach their respective electrodes. The increased charge carrier recombination lowers the fill factor, which has been indicated in the later session. All these parameters, including efficiency, short-circuit current density and fill factor are extracted from simulated current density versus voltage curves as shown in fig. 18b. Note that the open-circuit voltage almost does not change with variation of active layer thickness.

3.4 Dependence of Optimal Thickness on Mobility and Recombination

Above simulation on optimization of active layer thickness is based on given charge carrier mobilities and recombination. Here the dependence of optimal active layer thickness on mobility and recombination rate was further investigated. First, the recombination rate is kept the same as 0.5, the charge carrier mobilities for both electrons and holes are increased by one order of magnitude, that is, electron and hole mobility is increased to $6E-2 \text{ cm}^2/\text{Vs}$ and $1E-3 \text{ cm}^2/\text{Vs}$, respectively. As shown in fig. 19a, the

maximum efficiency happens at active layer thickness of ~70nm rather than ~60 when the charge carrier mobility increases, and this peak efficiency of 4.51 is higher than the maximum efficiency of 3.97 at active layer thickness of 60nm. As the charge carrier mobilities increase, the active layer thickness is allowed to increase for more light absorption while maintaining the recombination unchanged. Therefore, the maximum efficiency increases at a larger active layer thickness. Figure 13b shows the short circuit current increases as active layer thickness increases, while the fill factor presents the opposite trend. The maximum efficiency occurs at the best combination of short circuit current, fill factor and open circuit voltage. The open circuit voltage does not change except for active layer thickness of 30nm.

Second, the dependence of optimal active layer thickness on recombination rate was also studied. In this case, the charge carrier mobilities for electrons and holes remain the same as before, that is $\mu_n = 6E-3 \text{ cm}^2/\text{Vs}$ and $\mu_p = 1E-4 \text{ cm}^2/\text{Vs}$. As shown in fig. 19c, when the recombination rate decreases from 0.5 to 0.1, the peak efficiency of 4.49 is attained at active layer thickness of ~70nm. The reduced charge carrier recombination allows thicker active layer for more light absorption, leading to an enhanced efficiency. Again, the parameters of short circuit current and fill factor in fig. 19c are extracted from the simulated J-V characteristics shown in fig. 19d.

In a summary, the simulation study on active layer thickness concludes that optimal active layer thickness is related to mobility and recombination, which is the same as literature report^[23]. An increase of mobility and a reduction of recombination rate allow for a thicker active layer, which enhances light absorption for higher efficiency.

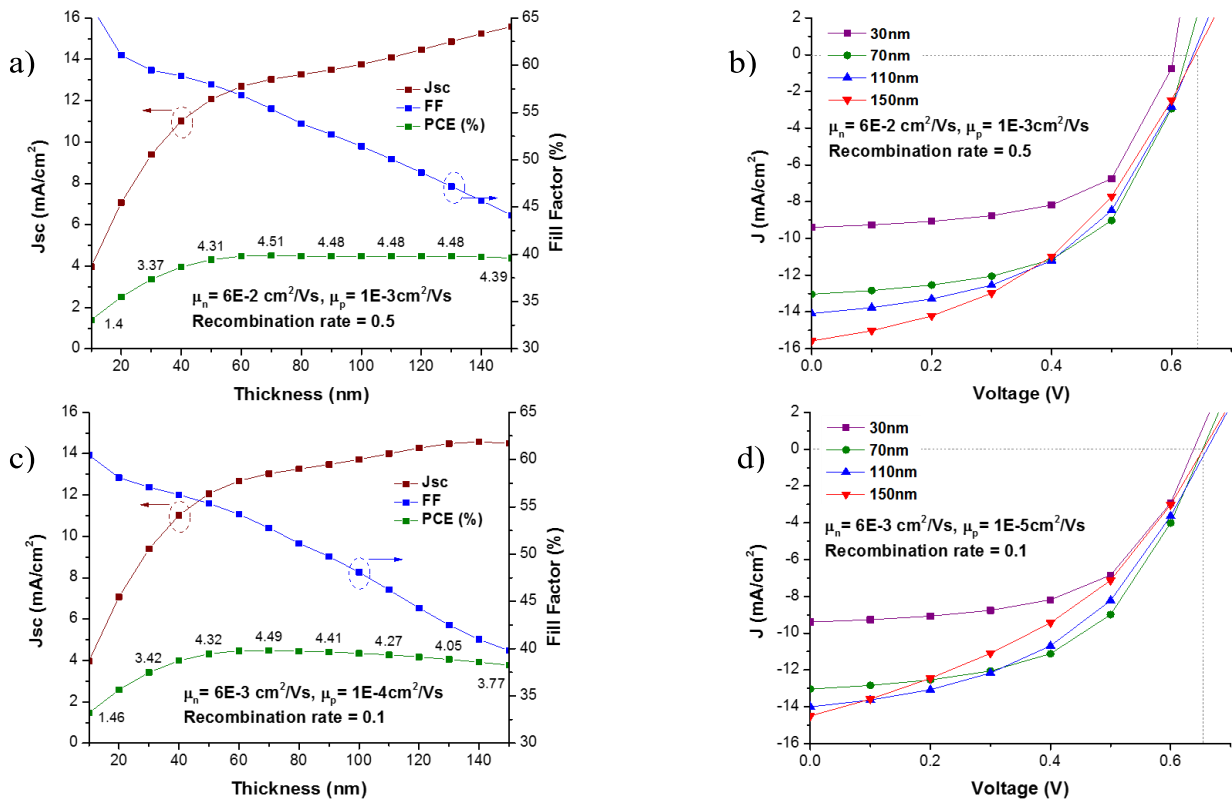


Figure 19: Dependence of optimal thickness on mobility and recombination a) PCE, J_{sc} , and FF versus thickness at increased mobility of $\mu_n = 6E-2 \text{ cm}^2/\text{Vs}$ and $\mu_p = 1E-3 \text{ cm}^2/\text{Vs}$ and constant recombination rate = 0.5; b) simulated J-V characteristics for parameter extraction of part a; c) PCE, J_{sc} , and FF versus thickness at reduced recombination rate of 0.1 and unchanged mobility of $\mu_n = 6E-3 \text{ cm}^2/\text{Vs}$ and $\mu_p = 1E-4 \text{ cm}^2/\text{Vs}$; and d) simulated J-V characteristics for parameter extraction of part c.

3.5 Effect of Recombination

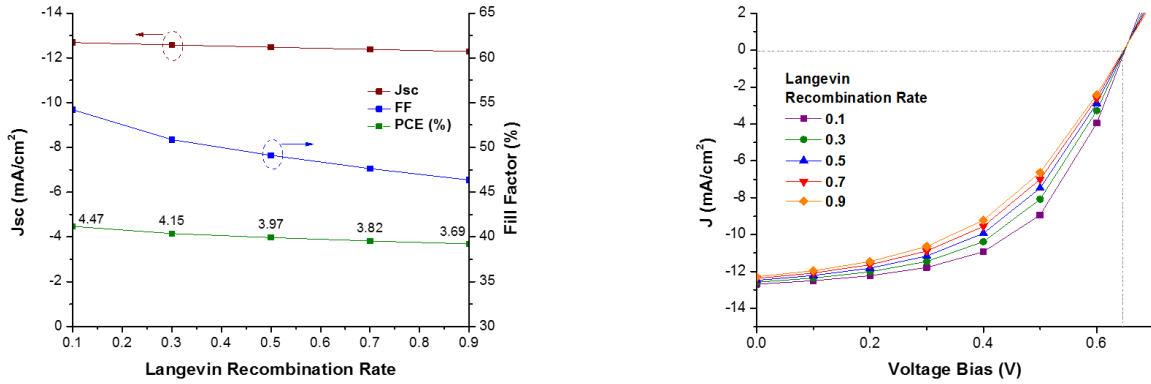


Figure 20: a) Effect of Langevin recombination rate on PCE, Jsc, and FF, b) simulated J-V characteristics as Langevin recombination rate varies.

Fig. 20a verifies the anticipation mentioned before that increased recombination causes reduced fill factor thereby overall power conversion efficiency. As the Langevin recombination rate increases from 0.1 to 0.9, the FF starts to drop from 53% at 0.1 to 47% at 0.9. Langevin recombination doesn't affect the short-circuit density by much and no influence on open-circuit voltage as shown in fig. 20b.

3.6 Effect of Hole Mobility in the Electron-donating Polymer

Usually hole transport in the electron-donating polymer is slower than electrons in electron-accepting fullerene derivative. Researchers try to improve the polymer crystallinity to increase the hole mobility thereby balancing the electron mobility. Here the active layer thickness is kept at the optimal value of 60nm. As shown in fig. 21a, an increase in hole mobility results in an increase in the device's efficiency primarily due to the enhancement of fill factor. The PCE reaches the peak value as hole mobility

approaches to the electron mobility ($6E-3 \text{ cm}^2/\text{Vs}$). Fig. 21b clearly shows fill factor increases as hole mobility increases.

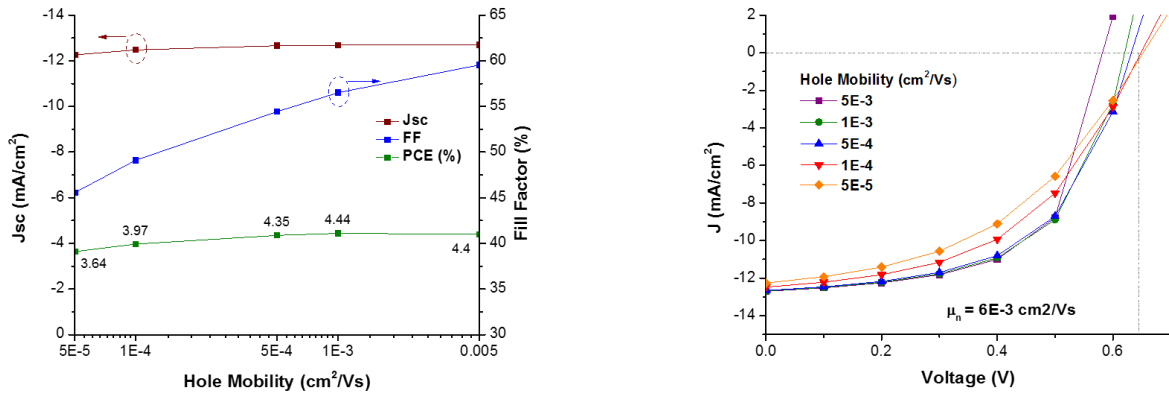


Figure 21: a) effect of hole mobility on power-conversion efficiency, short-circuit current density and fill factor, b) simulated J-V characteristic curves with different hole mobility.

3.7 Electron Transport Layer Selection

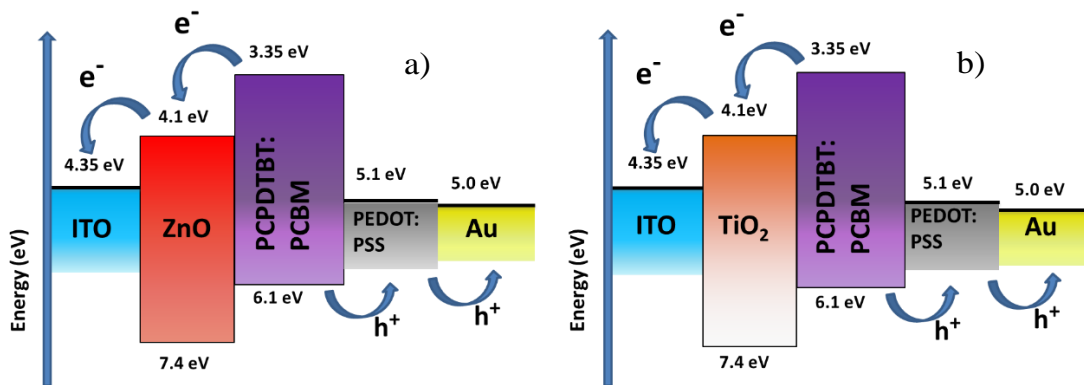


Figure 22: Energy band diagram of PCPDTBT: PCBM based organic bulk heterojunction solar cells using a) ZnO and b) TiO_2 as electron transport layer

In inverted ITO/ETL/PCPDTBT: PCBM/ PEDOT: PSS/ Au structure, both ZnO and TiO_2 can be used as electron transport layer. The energy band diagrams shown in fig. 22 indicate that ZnO and TiO_2 share the same LUMO energy level. The placement of

LUMO energy level ensures the smooth transport of electrons from PCPDTBT: PCBM active layer to the ITO electron collecting electrode. On the other hand, the low HOMO energy level of ZnO and TiO₂ also serves as a hole blocking layer to ensure that holes do not travel to the ITO electrode.

Table 4: Device parameters for both ZnO and TiO₂ electron transport layers

Electron Transport Layer	Electron Mobility (cm ² /Vs)	Work Function (eV)	Voc (V)	Jsc (mA/cm ²)	Fill Factor (%)	Efficiency (%)
ZnO	30	4.1	0.8918	-14.419	35.26	4.53
TiO ₂	3.0E-4	4.1	0.9617	-14.5985	29.71	4.17

Although there is no difference in terms of energy level between ZnO and TiO₂, electron transport in ZnO is much better than in TiO₂. Based on mobility difference, simulation was done to study the effect of electron mobility in ETL on the performance. As indicated in Table 4 inverted organic solar cells with ZnO as electron transport layer have enhanced fill factor compared with those using TiO₂ as ETL, which results in improved efficiency. Therefore, it is safe to conclude that ZnO is a better choice serving as an electron transport layer due to its much higher electron mobility than TiO₂, even though there is no difference in LUMO energy level.

CHAPTER 4. CONTROLLABLE GROWTH OF ANNEALING-FREE PEROVSKITE THIN FILMS VIA A SEEDED APPROACH

Organometal halide perovskites solar cells (PSCs) have recently sparked extensive attention due to their high carrier mobility for long diffusion length, suitable optical bandgaps for strong absorption of light^[9,48–55]. One of the main challenges in fabricating high yield PSCs is to control the morphology and crystallinity of perovskite films^[56–58]. Various techniques for fabricating the perovskite thin films have been documented. One-step spin-coating approach, directly spin-coating of premixed lead iodide (PbI_2) and methylammonium iodide ($\text{CH}_3\text{NH}_3\text{I}$, MAI), is the most convenient to implement, but the resulting films usually have poor surface uniformity and coverage^[59–62]. The two-step deposition approach, in which perovskite thin films are formed by sequentially depositing PbI_2 and MAI, generates perovskite solar cell devices with high efficiency with good reproducibility^[63–65]. Other methods, such as vapour-assisted deposition^[53,66–68], solvent engineering^[69–72], and compositional tuning^[73,74], have all been reported to improve perovskite thin film fabrication and device efficiency.

Herein, a new seeded crystallization technique for perovskite deposition with controlled morphology and grain size is reported. Specifically, a solution of PbI_2 was spin-coated on a substrate, and a low concentration solution of MAI was dropped onto the PbI_2 film to form perovskite seeds before the spin-coating of high concentration solution of MAI. The seeded nucleation and growth leads to dense and uniform films exhibited controlled crystal grains.

The schematic illustration of seeded layer growth is shown in fig. 23 below.

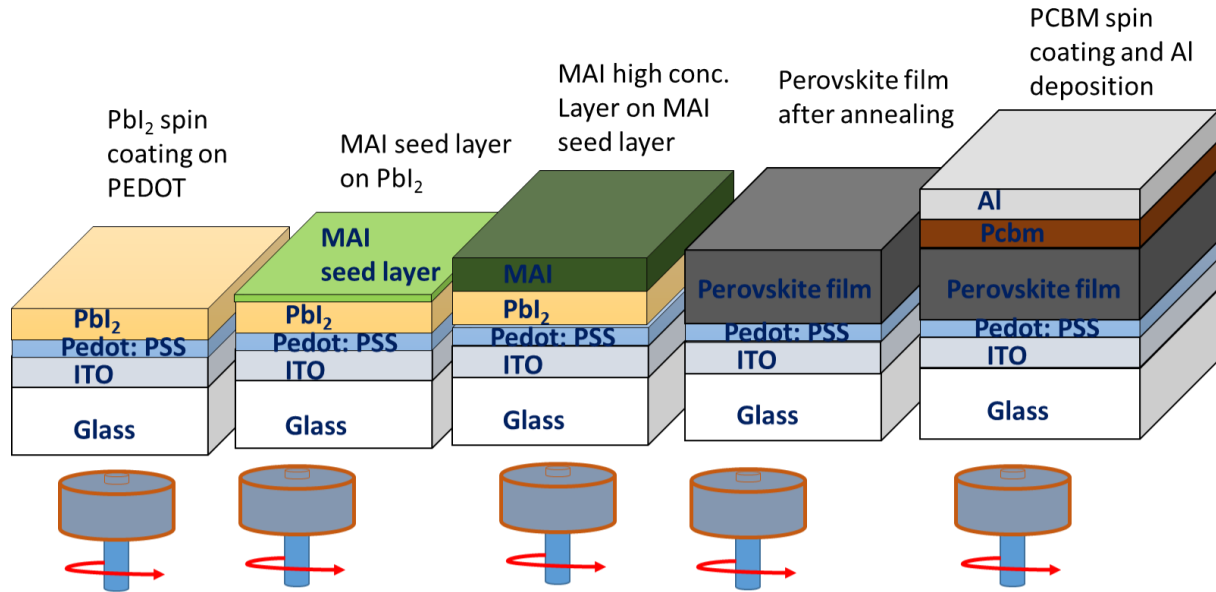


Figure 23: Schematic illustration of seeded growth of perovskite thin films and device fabrication.

For a typical seeded deposition of perovskite, PbI₂ and MAI were dissolved in dimethylformamide (DMF) and 2-propanol (IPA), respectively. 100 μ L of 1M PbI₂ was spun onto poly(3,4-ethylenedioxythiophene): poly(styrenesulphonate) (PEDOT: PSS) covered indium tin oxide (ITO) glass, followed by dropping 200 μ L of 1 mg/mL MAI on the surface of PbI₂ thin film for 1 minute. The remaining MAI solution was spun off and followed by dropping a high concentration of MAI solution (10 mg/mL) for 1 minute before spin-coating. The yellowish colour of PbI₂ did not change after the addition of low concentration MAI solution. However, a dark brown colour appeared immediately after the introduction of high concentration MAI solution, indicating the formation of

perovskite crystals. Fig. 24 shows the scanning electron microscopy (SEM) images of PbI_2 thin film (fig. 24a), PbI_2 thin film with perovskite seeds (fig. 24b), perovskite thin film obtained by seeded growth (fig. 24c), and perovskite thin film made from premixed PbI_2 and MAI solution (fig. 24e). As a comparison, perovskite thin films were fabricated by using a well-established inter-diffusion method^[12]. Fig. 24a reveals a very compact, dense and continuous PbI_2 film, while the PbI_2 /seed film (fig. 24b) is porous due to the reaction between PbI_2 and MAI, and the subsequent formation of MAPbI_3 seeds.

Continuous and pinhole free perovskite thin film is formed after the addition of high concentration MAI, as shown in fig. 24c and 24d. In contrast to the particle-like grains of perovskite thin film obtained from seeded growth, the perovskite film made from premixed PbI_2 and MAI blend solutions is composed of fibre like structure, with large amount of pin holes and poor surface coverage, as shown in fig. 24e. For the inter-diffusion method, the as-obtained perovskite thin film is composed of perovskite particles, as shown in fig. 24f. However, the surface of the film is less smooth and dense.

To further investigate the seeded growth of perovskite thin film, X-ray diffraction (XRD) characterization was performed, as shown in fig. 25a. The PbI_2 film shows a strong peak at 14.6° . After the addition of low concentration MAI solution, the resultant thin film generates an XRD pattern basically the same as the pattern of pure PbI_2 , which may indicate that the amount of perovskite seeds is very small and amorphous in nature. In the XRD pattern of perovskite thin film formed by seeded growth, the peak at 14.6° completely disappears, suggesting the fully conversion of PbI_2 into perovskite. There is also no peak shown at 12° , the characteristic peak of MAI, indicating that there is also no residue of MAI.

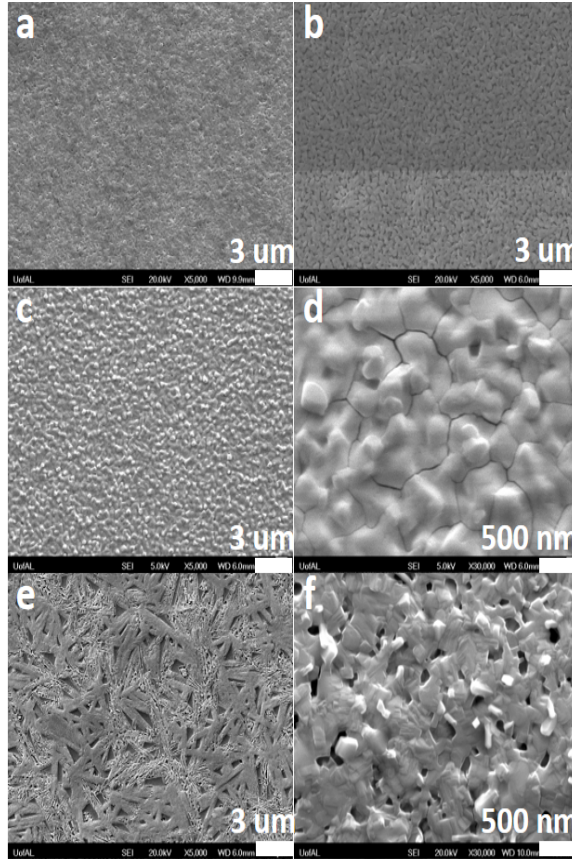


Figure 24: Fig. 1 SEM images of a) the PbI₂ film, b) the perovskite seed layer, c) the perovskite film obtained by seeded growth, d) high magnification image of perovskite film by seeded growth, e) the perovskite thin film obtained from the premixed PbI₂ and MAI solution, and f) regular interdiffusion method without seeding layer

To monitor the growth of seeded growth of perovskite, UV-vis measurements were conducted, with results shown in fig. 25b. Both PbI₂ and PbI₂/seed thin films show a strong peak at 496 nm. The difference of absorption intensity between PbI₂ and PbI₂/seed may be attributed from the thickness difference. For perovskite thin films obtained by seeded growth, UV-Vis spectra show an absorption edge at 760 nm. Surprisingly, the annealed perovskite thin film generates basically a same spectrum like the unannealed

thin film. In contrast to the interdiffusion method, in which the absorption increased during thermal annealing of perovskite thin film, our method seems to produce thin film without the necessity of annealing.

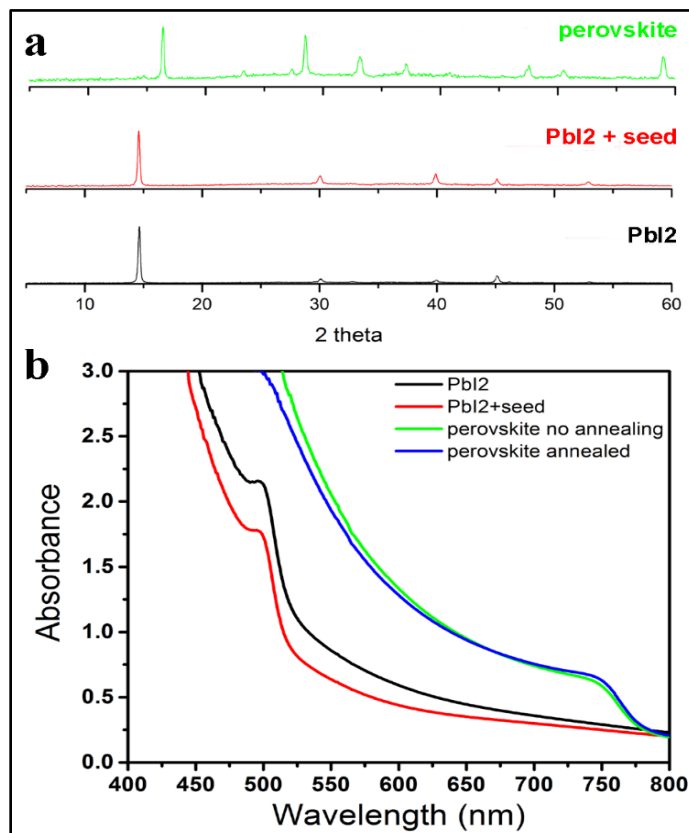


Figure 25: XRD patterns of PbI₂, PbI₂ with perovskite seed, and the perovskite thin film formed by seeded growth. 3b) UV/Vis spectra of PbI₂, PbI₂ with seed, perovskite thin film obtained by seeded growth with or without thermal annealing.

To optimize the thin film fabrication, extensive study was carried out using SEM and XRD measurements. To begin with, investigation of the influence of first step MAI by varying its concentration from 0.5 mg/mL, 1 mg/mL, 1.5 mg/mL, to 2 mg/mL while keeping the concentration of the second step MAI constant was conducted, with results shown in fig. 26.

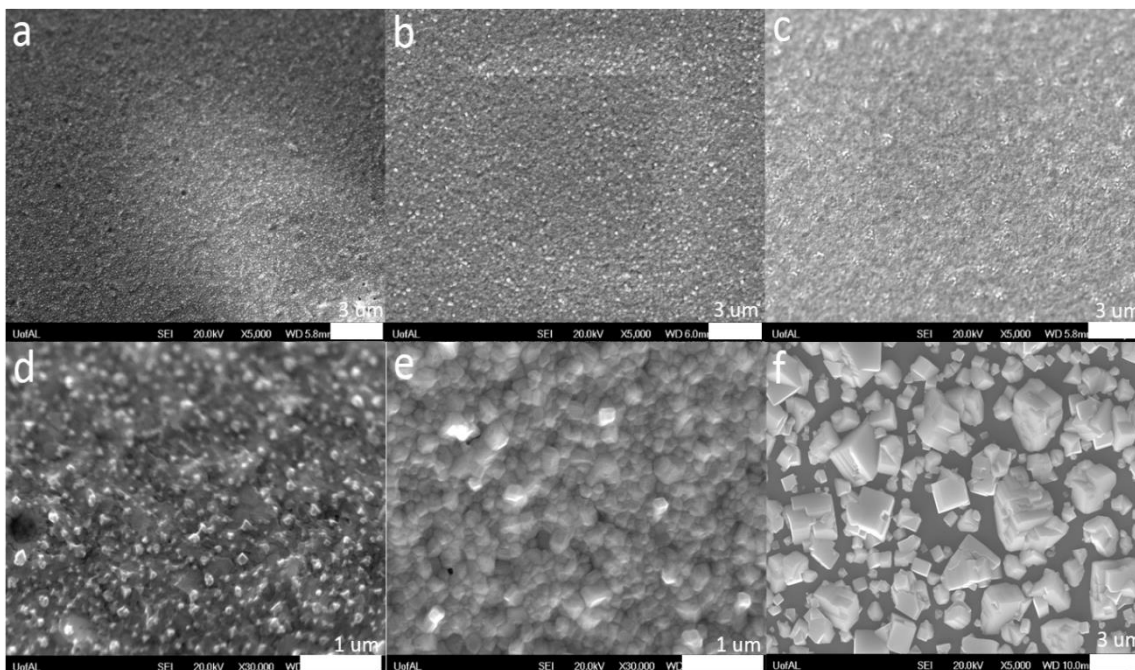


Figure 26: SEM images for first MAI layer optimization. For the second step of MAI, concentration was constant at 10 mg/mL. For the first step MAI, concentration was varied from 0.5 mg/mL (a & d), 1 mg/mL (b & e), 1.5 mg/mL (c), and 2 mg/mL (f), respectively.

Results show the concentration of first step MAI is an important factor to achieve uniform and dense perovskite thin films. When the concentration of first step MAI is 0.5 mg/mL, besides the formation of a dense and pinhole free thin, it also generates many small particles. When the concentration of first step MAI is 1.5 mg/mL, it generates some large clusters. When the concentration increases further to 2 mg/ml, the concentration is high enough to trigger the formation of perovskite particles, instead of dense thin film with seeds. The best concentration of first step MAI is 1 mg/mL, which gives the perovskite thin with the most uniform morphology.

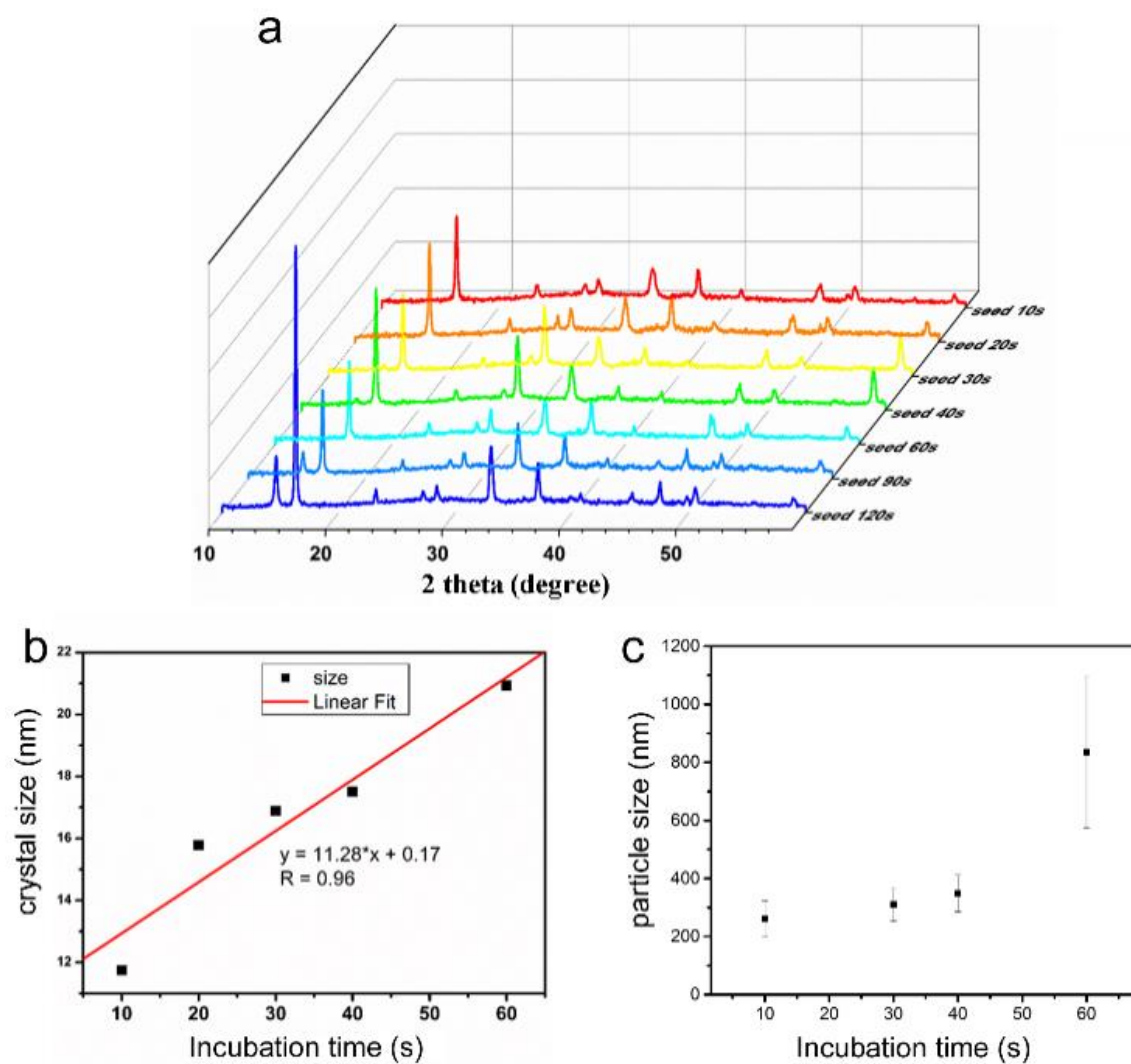


Figure 27: a) XRD patterns of perovskite thin film with different incubation time of PbI₂ and first step MAI solution. b) grain size analysis by using Scherrer equation. The full width at half maximum at 33.6° was employed for the calculations

Second MAI step was further optimized by adjusting its concentration from 10, 20, and 30 mg/mL (SEM results shown in fig. 28). It was found that perovskite thin films with best morphology were fabricated at concentration of 10 mg/mL, while high concentration of MAI will generate large number of big perovskite particles. Through this optimization, it was determined that 1 mg/mL of first step MAI and 10 mg/mL of second step MAI

would produce uniform, dense, and pinhole free perovskite thin films without unwanted particles or clusters on the surface.

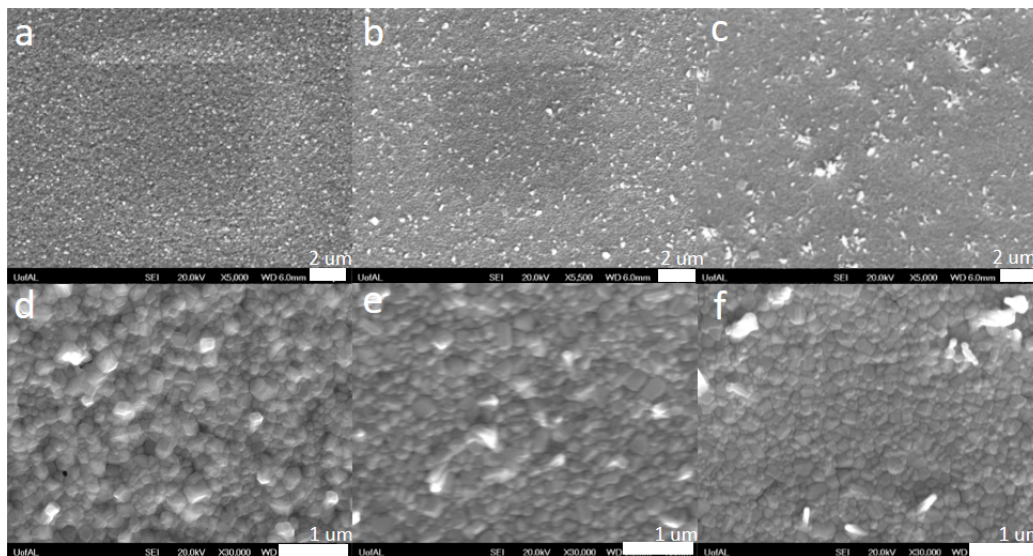


Figure 28: SEM images for the second MAI layer optimization First step of MAI, concentration was constant at 1 mg/mL Second step MAI, concentration varied from 10 mg/mL (a & d), 20 mg/mL (b & e), 30 mg/mL (c & f)

Furthermore, it was observed that the grain size of perovskite thin film can be well controlled by adjusting the sitting time of first MAI solution on the top of PbI_2 thin film, while keeping the deposit parameters for the second step MAI constant. As shown in fig. 27a, XRD patterns indicate that the conversion of PbI_2 and MAI into perovskite could be affected by the incubation time of first step MAI solution and PbI_2 films. When the incubation time is not more than 1 minute, pure perovskite without both PbI_2 and MAI residues could be obtained. However, when the incubation time is too long, the PbI_2 could not fully convert into perovskite, evidenced by the remaining peak at 2θ 14.6° . To probe the possible reason, a series of XRD measurements were carried out on the interaction of PbI_2 and first step MAI, with results shown in fig. 29.

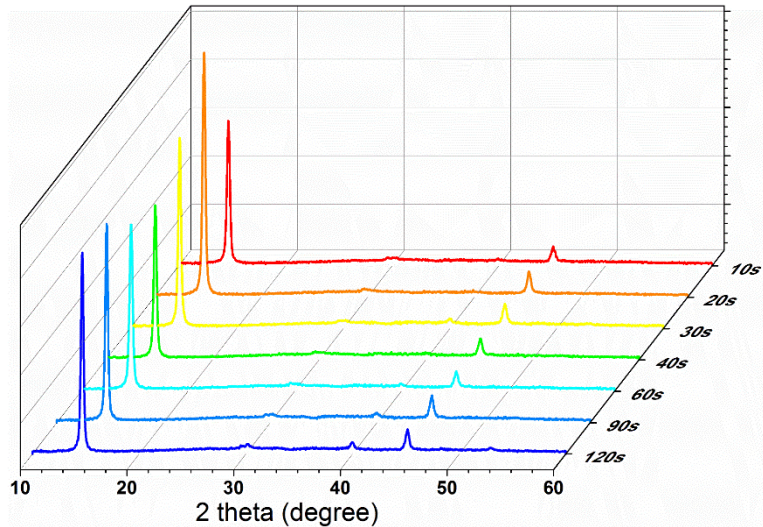


Figure 29: XRD patterns of PbI_2 with seeding layers as a function of first step MAI solution sitting time. Without 2nd MAI)

For incubation time, no more than 1 minute, the XRD patterns of PbI_2/MAI shows no difference from the XRD pattern of pure PbI_2 . However, for longer time of incubation PbI_2 with MAI (90 s and 120 s), the peak at 2 theta 39.5° becomes increasingly stronger, suggesting some degree of change of PbI_2 crystal structure. The exact reason and mechanism is still elusive and subject to ongoing investigation. At this stage, it was assumed that the long interaction between first step MAI and PbI_2 might produce large amount of amorphous perovskite seeds or cause the rearrange of PbI_2 crystal structure, which hinders the diffusion of second layer MAI into PbI_2 and causes the incompleteness of PbI_2 conversion. Based on XRD patterns of pure perovskite in fig. 25a, the crystal size was analysed by using Scherrer equation. The crystal size of perovskite thin film increases from 11.7 nm, 15.6 nm, 16.9 nm, 17.5 nm, to 20.9 nm when the incubation changes from 10s, 20s, 30s, 40s, and 60s, respectively. Further regression analysis shows that the crystal size is linear to the sitting time of MAI solution on the surface of PbI_2 thin film, as shown in fig. 27b. This is an encouraging finding, as it gives a clue to fine tune

the crystal size of perovskite thin film by controlling the incubation time of PbI_2 and first step MAI.

The increase of grain size with the elongation of incubation time is in accordance with SEM observations. As can be seen from the SEM images in fig. 30, the size of perovskite particles which make up the thin film increases. Randomly, 100 particles in the SEM images were selected to analyse the size and size distribution. The particle size is 261 ± 62 nm, 311 ± 58 nm, 349 ± 63 nm, and 835 ± 260 nm, corresponding to sitting time of 10s, 30s, 40s, and 60s, respectively, as shown in fig. 27c. The trend of particle size is in line with the trend of that obtained from XRD analysis.

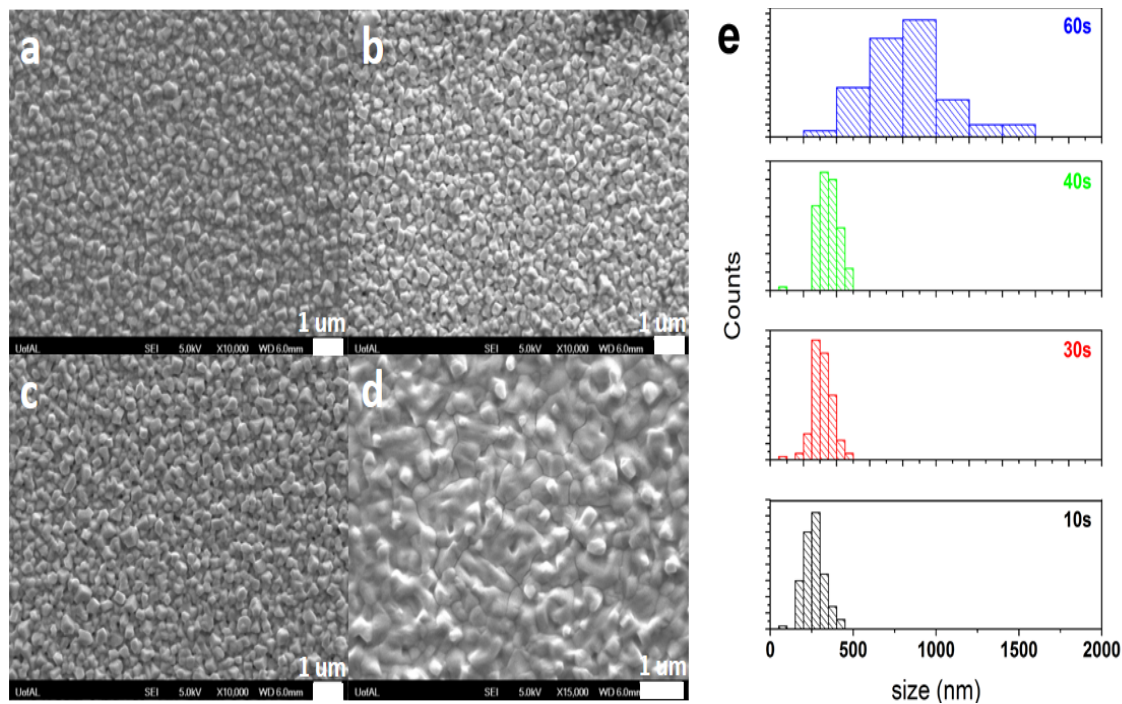


Figure 30: Incubation time optimization for perovskite thin films Incubation time (low concentration MAI solution on top of PbI_2 before spin-coating) dependent formation of perovskite thin film. a) 10s, b) 30s, c) 40s, d) 60s, and e) histogram of particle size of perovskite thin film determined from SEM images.

It should be noted that the seeded method presented here is different from the interdiffusion method reported by Huang et al^[12]. In the interdiffusion method, perovskite thin film is formed by the solid-state reaction of MAI thin film and the underneath PbI_2 at a temperature of 100 °C for certain a period. To obtain pure perovskite thin film, a thickness ratio of 1.4: 1 for the MAI: PbI_2 layer is needed to form a stoichiometry iodine perovskite. For our method, the addition of MAI was divided into two steps. In the first step, the low concentration MAI solution reacts with PbI_2 to form a seeded layer of MAPbI_3 , which grows into perovskite thin film upon the addition of high concentration MAI solution. Without the first step MAI, however, the high concentration MAI reacts too fast with PbI_2 such that a dense perovskite thin film will be formed immediately upon the addition of MAI which hinders the diffusion of MAI and causes the incompleteness of PbI_2 conversion, as demonstrated by Huang et al. With the help of low concentration of MAI solution, the compact PbI_2 thin film rearranges and becomes more porous, which allows the easy diffusion of liquid MAI solution into PbI_2 network, and the liquid-solid reaction in this case can be greatly enhanced (in just 1 minute) and complete without resorting to thermal annealing.

The performance of the PSCs was evaluated by means of current density versus voltage (J–V) measurements under simulated air mass (AM) 1.5 G (100 mW cm^{-2}) irradiation in ambient air. The device based on the seeded perovskite film had an open-circuit voltage (V_{OC}) of 0.9 V, a short-circuit current density (J_{SC}) of 23.12 mA cm^{-2} , a fill factor (FF) of 69%, and an overall power conversion efficiency of 12.87% in the forward sweep direction

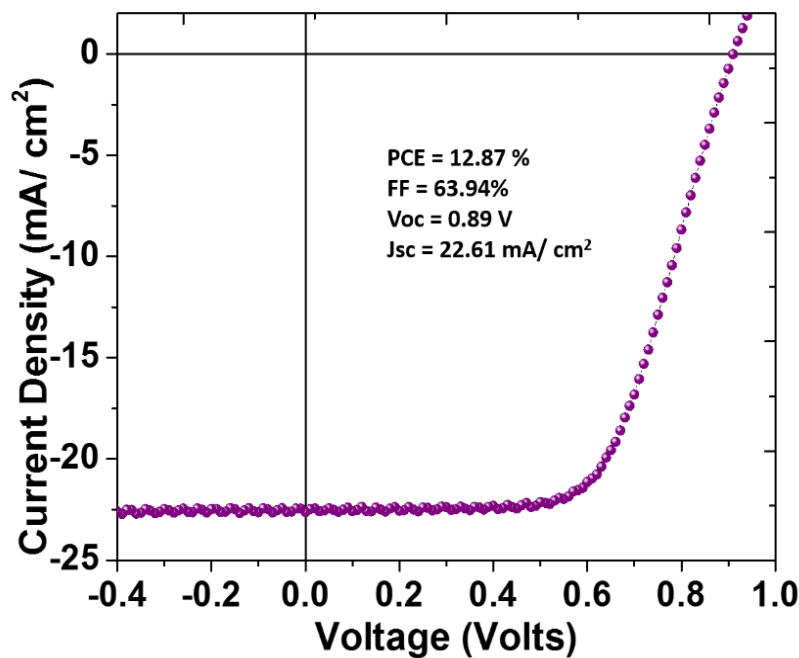


Figure 31: Performance of the perovskite device.

In conclusion, a new seeded-crystallization technique for deposition of perovskite films was demonstrated. The seeded layer of perovskite induced dense and uniform perovskite films with controlled grain size and morphology, and this technique can be used to reproducibly generate high-quality perovskite films. PSCs fabricated with seeded-perovskite films showed a high power conversion efficiency of 12.87%. From the perspective of global photovoltaic commercialization, this seeded-crystallization approach to the deposition of perovskite film can facilitate the fabrication of efficient and low-cost photovoltaics.

4.1 Experiments

Materials:

PbI₂ (beeds, 99.9999%) was purchased from Sigma Aldrich. Methylammonium iodide (MAI) was purchase from Dyesol. 2-propanol alcohol (IPA) and

Dimethylformamide (DMF) were purchased from VWR. PEDOT: PSS and PCBM were purchased from Alfa Aesar. All the chemicals were used as-received without any further purification.

Precursor solution preparing and PbI_2 and MAI layer deposition:

PbI_2 was dissolved in DMF at the concentration of 1 mol/L. MAI was dissolved in IPA with different concentrations 0.5 mg/mL to 30 mg/mL. Both solutions were heated at 70 °C overnight to make sure both MAI and PbI_2 can be fully dissolved. The PbI_2 solution was spun on PEDOT: PSS substrate at 70 °C at 4,000 round per second (rpm) for 30 s. The low concentration MAI solution was dropped onto the surface of PbI_2 for 1 minute and remaining solution was spun off. The high concentration MAI solution was subsequently dropped onto the PbI_2 /seed film for 1 minute and remaining solution was spun off. The resultant perovskite thin films were dried at 100 °C for 5 to 10 min.

Film characterization:

XRD measurements were performed with a Bruker D8 X-ray diffractometer with a conventional cobalt target X-ray tube set to 40 KV and 30 mA. The single path absorption was measured using a Beckman D 800 UV-Visible spectrometer. SEM images were taken by using a Joel 7000 Scanning Electron Microscope.

CHAPTER 5. POLYMER ADDITIVE ASSISTED FABRICATION OF ULTRA-SMOOTH AND STABLE PEROVSKITE THIN FILMS

Methylammonium lead trihalide perovskite has been emerging as a promising material in photovoltaics because of their high absorption coefficient, long carrier life time, and micrometer diffusion length^[75–77]. There are mainly two kinds of well documented device architectures: mesoporous and planar heterojunctions^[12,59,63,66]. In the mesoporous architecture, high temperature annealing is usually necessary to produce a TiO₂ layer with good crystallinity, whereas planar heterojunction-based devices can be fabricated at low temperature. Unlike devices with mesoporous structure, in which the perovskite material can readily infiltrate into the porous matrix, planar perovskite solar cell devices usually suffer from pinhole and non-uniform coverage of perovskite thin films on the top of hole-transport layers. The pinhole and non-uniformity are the major issues that are responsible for the poor device performance^[78]. Controlling the nucleation and formation of perovskite thin film in planar architecture is thus a main challenge for developing high-performance devices^[79–83].

Considerable efforts have been dedicated to control the morphology and crystallinity of perovskite thin films^[84–87]. The choice of solvent^[70,71], annealing temperature^[88–90], moisture^[13,91–93], and composition^[74,94–96] have been proven as effective measures to tune the nucleation and growth of perovskite thin film. Recently, incorporation of additives in the pre-mixed perovskite solution process has been demonstrated as a facile way to improve the thin film coverage and crystallinity^[24,29,32–34,93,97–101]. Several additives, including

NH_4Cl ^[32], 1-chloronaphthalene^[98], hydroiodic acid (HI)^[99], hydrochloric acid^[102], and alkali metal halides^[29] have been implemented to fabricate smooth, continuous, and uniform perovskite thin films, which showed significantly enhanced device performance.

Here, the effects of Polyamidoamine (PAMAM) dendrimers as a kind of powerful additive on the regulation of perovskite thin film nucleation and growth were investigated. PAMAM was incorporated into the blend solution of PbI_2 and MAI to tune the morphology and crystallinity of the perovskite films. The amine rich PAMAM additive chelates strongly with Pb^{2+} ions during film formation. The nucleation and growth of perovskite thin film thus can be well mediated and regulated by the amount of PAMAM additive. This polymer additive assisted one-step method represents a facile route for the controllable fabrication of perovskite thin films for planar PSCs with high performance and stability.

Based on the XRD patterns of perovskite thin films with different ratio of PAMAM shown in fig. 32, it was found that the presence of PAMAM regulates the nucleation and growth of perovskite thin films. As the amount of PAMAM increases from 1% to 6%, the ratio of peak intensity at 16.5° and 32.8° decreases, suggesting the inhibition of nucleation and growth of perovskite along the (110) direction. The effect of annealing time on the nucleation of perovskite thin film with PAMAM polymers was also investigated.

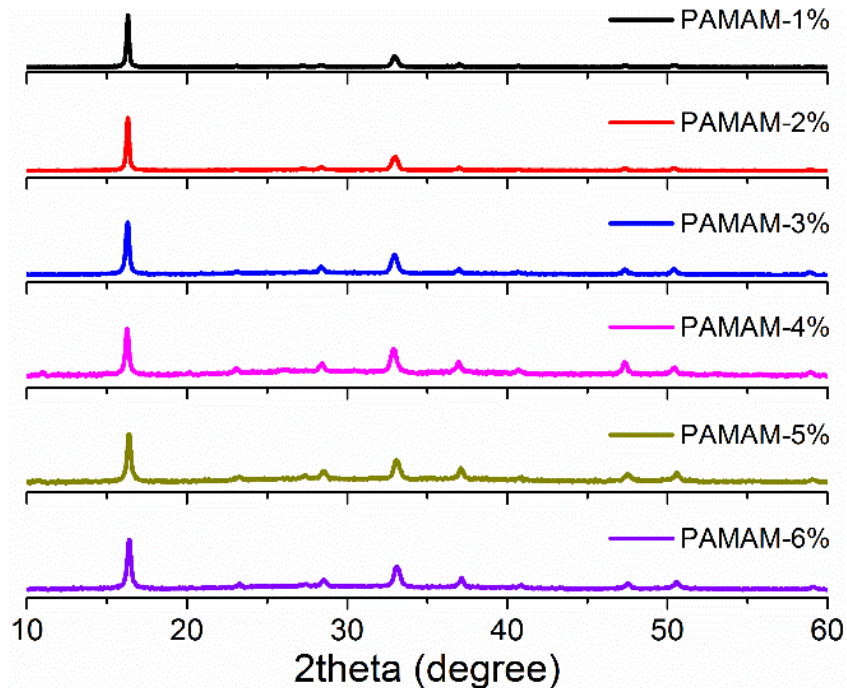


Figure 32: XRD patterns of perovskite thin films with different ratio of PAMAM (after annealing)

The precursor solution contains equal moles of PbI₂ and MAI, thus ideally there would be no peaks from both MAI and PbI₂ if all the precursor converts into perovskite MAPbI₃. However, MAI peaks (degree 11) were seen at short period time of thermal annealing (10 min and 20 min), indicating a strong interaction between PbI₂ and PAMAM, which competes with MAI for reacting with Pb²⁺. After 30 minutes of thermal annealing, all the MAI peaks disappear and generate pure thin films of perovskite.

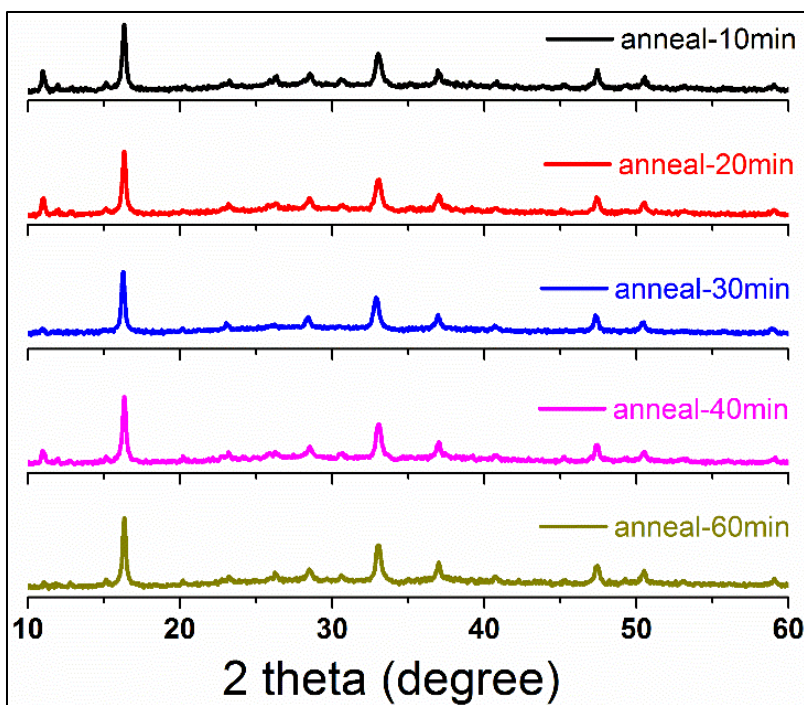


Figure 33: XRD patterns of PAMAM-perovskite thin films at different annealing time. The concentration of PAMAM was 4%.

Furthermore, different solvents have been used to wash the perovskite film while being spin coated to improve the surface morphology and remove the residues of unreacted MAI and PbI_2 . From fig. 34, the magnification SEM images show the films flushed with toluene yielded bigger crystals while maintaining the uniformity of the film.

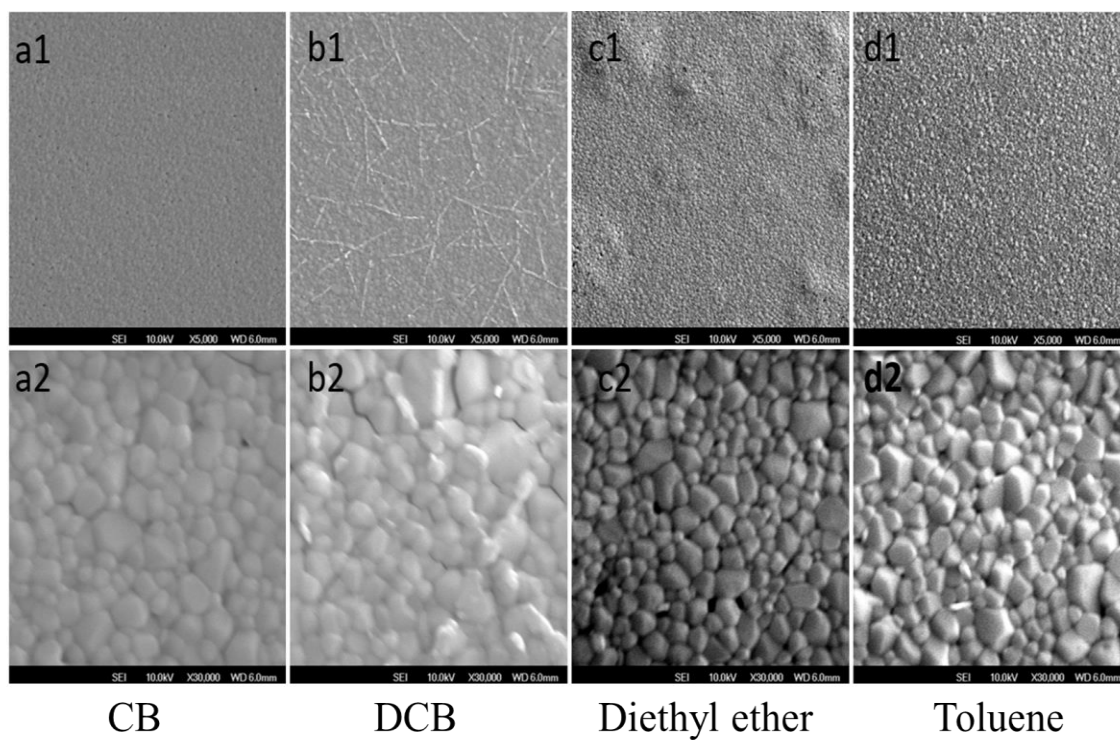


Figure 34: SEM images of Perovskite-PAMAM thin films with different solvent wash: a1) a2) chlorobenzene, b1) b2) dichlorobenzene c1) c2) diethyl ether, d1) d2) toluene

XRD was carried out to investigate the crystallinity of the films washed with CB, DCB, diethyl ether and toluene solvents. It was found out that all the films showed identical perovskite peaks.

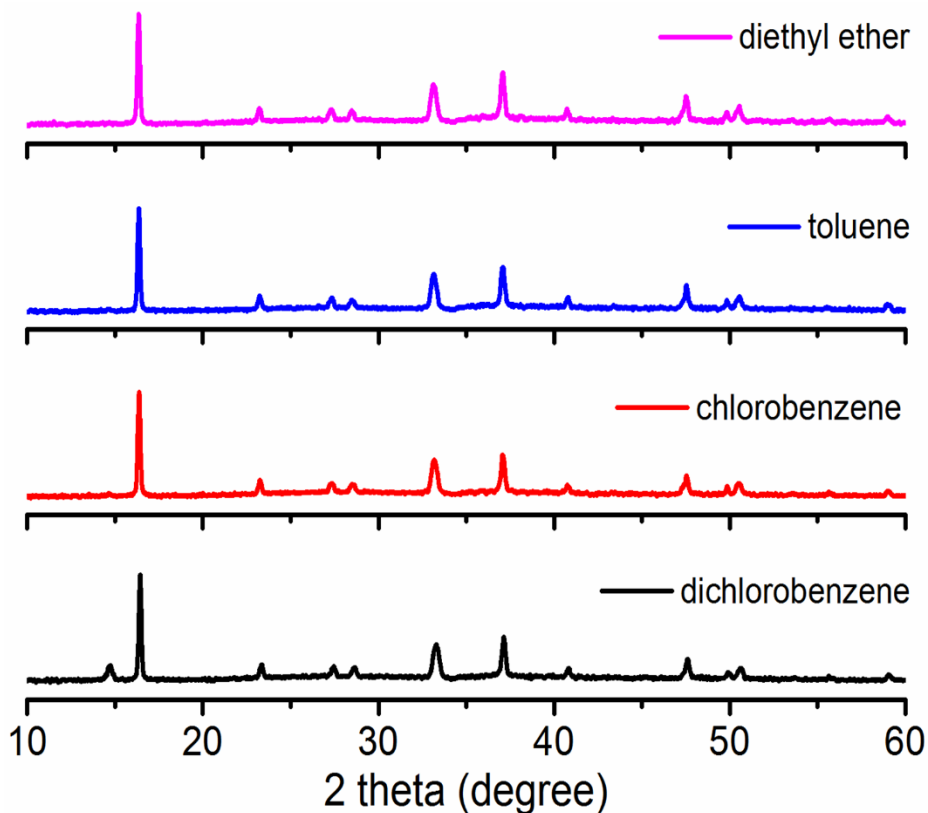


Figure 35: XRD patterns of perovskite thin films with different solvent used for perovskite film washing.

Based on the XRD patterns of perovskite thin films with 1%wt of PAMAM annealed at different conditions, it was found that the lamp annealing notably promotes the nucleation and growth of perovskite thin films. For perovskite thin film with PAMAM annealed with hot plate, long period of time is needed to fully convert the PbI_2 and MAI into perovskite. Previously, it was found that on annealing perovskite thin film on hot plate for 30 minutes, characteristic MAI peak at 12° was observed. Only with 60 minutes or longer time of annealing, pure perovskite thin films free of both PbI_2 and MAI residues were obtained. Surprisingly, the growth of pure perovskite was achieved by 250 W lamp annealing for as short as 30 seconds when using wood as the sample holder. For glass and metal sample holders, full conversion at 1 minute and 3 minutes of lamp annealing was achieved, respectively.

As mentioned earlier, the addition of polymer additive is believed to increase the device stability and slow down the degradation of films. From fig. 36 degradation of different concentrations of PAMAM over a period of time was observed.

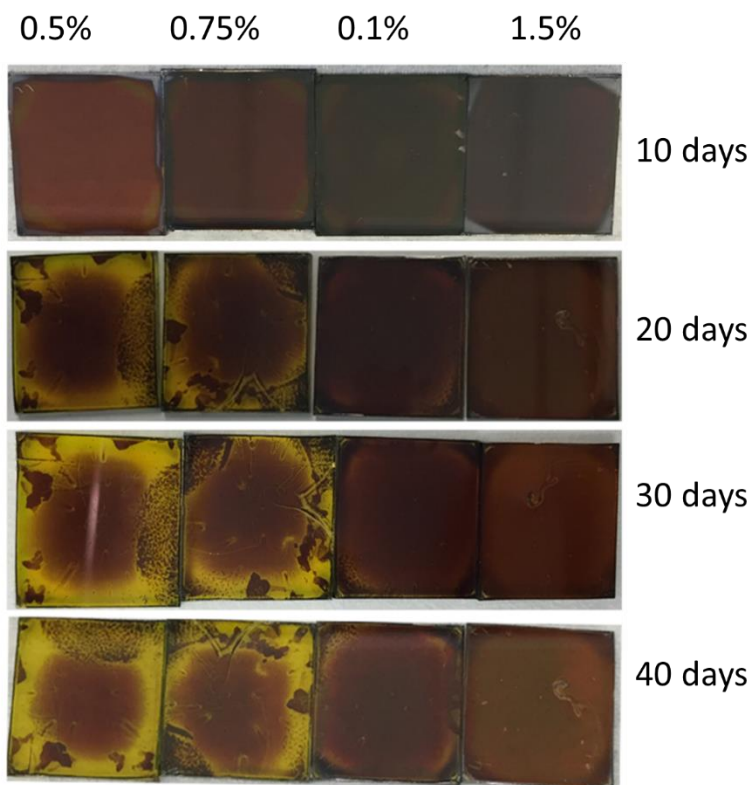


Figure 36: Optical images of the film degradation with different concentration of PAMAM.

It can be inferred the concentration of PAMAM can control degradation and improve the stability of perovskite thin film at ambient conditions without any encapsulation and protection. This enhanced stability can be attributed from the following two aspects of PAMAM as a powerful additive. One is that the amine functional group of branched PAMAM interacts with perovskite thin film (possible interactions) and promotes the formation of a highly-crosslinked structure, thus prevents the separation of PbI_2 and MAI

when moisture is presented. The other one is that the long polymer chain can also wrap the grains of perovskite, thus increase the stability.

5.1 Rapid IR lamp annealing of perovskite thin films

In addition to deposition, annealing step also plays a critical role to ensure optimal film crystallization thereby attaining high quality perovskite films. Typically, a hot plate is used for thermal annealing of perovskite films at 100°C for 1 hour. Such long annealing time makes the fabrication of perovskite solar cells less efficient.

Herein, a new method of annealing using incandescent infrared (IR) heat lamp is introduced and developed. The electromagnetic radiation from IR heat lamp is mainly in longer infrared wavelengths with some visible light spectra. Infrared energy is well-known for heating. Once IR light is absorbed by perovskite thin film, it stimulates vibrational modes within the molecules and heat up the material. IR annealing possesses many advantages over hot plate heating, including rapid heating and uniform temperature distribution. Results show that through IR heating, the perovskite solar cells could reach required annealing temperatures of 100 °C in less than 3 minutes, much faster than hot plate annealing for 1 hour. The perovskite solar cells from 250 W infrared lamp annealing for 30 seconds on wood holder show efficiency of 10.3% as compared with PCE around 9% from hot plate annealing for 60 minutes. Therefore, the facile IR lamp annealing paves the way for speedy manufacturing of perovskite solar cells thereby reducing the fabrication cost while maintaining the device performance.

ITO glass substrates were first cleaned using detergent, followed by acetone and isopropanol (IPA) sonication for 40 minutes, respectively. Substrates were then oxygen

plasma treated for 30 minutes to increase surface energy for better wetting of PEDOT on ITO surface. After drying on a hot plate at 80 °C for 5 minutes, the PEDOT: PSS was spin coated at 5000 rpm (revolutions per minute) for 45 seconds and annealed at 140 °C for 15 minutes.

To prepare perovskite precursor solution, 1M (precisely 461 mg/mL) PBI_2 and 1M (159 mg/mL) MAI were dissolved in anhydrous dimethylformamide (DMF) solvent, and 1 wt% PAMAM dendrimer was added to this precursor solution. The resulting blend solution was then spin coated on the top of PEDOT: PSS layer at 2000 rpm for 10 sec and 4000 rpm for 45 sec to attain perovskite film thickness around 350nm, which is optimal thickness to balance light absorption and charge transport^[103]. During the spin coating of the precursor solution, about 0.5 mL of toluene solvent was dropped on the substrate to wash the perovskite active layer. The underlying principle is that toluene solvent has lower boiling point (110.6 °C) than DMF (153 °C), toluene washing will drive the DMF out of the perovskite film through evaporation, resulting in smooth and shiny thin films.

Thermal annealing is a critical step for formation of quality perovskite films with high crystallinity and desired morphology. Usually hot plate annealing at 100 °C for 60 minutes is used in the lab. Another method for quick thermal annealing was developed, that is, infrared lamp annealing. With lamp annealing approach, an incandescent 250W IR heat lamp was used as a heating source. After spin-coating of perovskite layer, substrates were placed on a holding plate, which is either wood or glass supporting plate. Samples on the wooden base were annealed under the lamp for 30 seconds and 1 minute, respectively, and sample substrate on the glass base were annealed for 3 minutes. The choice of annealing time is based on study of sample temperature versus heating time on

different holding plates, which will be detailed in results and discussion section. During lamp annealing, the distance between the top of the supporting plate and the bottom of the lamp was maintained about 3 inches and undisturbed throughout the annealing process. After thermal annealing, a 20mg/mL PCBM in IPA solvent was spin coated at 2000 rpm for 30 s and annealed at 100 °C for 30 minutes. Finally, the perovskite solar cells were completed by thermal evaporation of 100 nm Al at 2Å^o/second evaporation rate.

Annealing of perovskite films using an incandescent IR lamp holds some major advantages over typical hot plate heating. First of all, the lamp annealing is more uniform because the radiation created by the lamp has a considerably even distribution of intensity, while the substrate temperature on the hot plate depends on the location, where central area typically has higher temperature than surrounding outside regions. Since the morphologies of perovskite films are sensitive to the annealing temperature, a slight temperature variation from hot plate annealing could cause wide distribution in device performance. Second, unlike hot plate annealing where heating is through thermal conduction, the radiation emitted by the lamp directly raise film temperature. Upon absorption, the infrared part of radiation excites vibrational modes in the molecules, while the photons in UV and visible light spectrum will boost certain electrons to higher energy levels. Due to no extraction of charge carriers, the electrons will decay to lower energy levels and dissipate their energy as phonons, which is also thermal energy. By increasing the lamp power, huge number of photons can bring the thin films to the intended temperature in a much short annealing time. Finally, with the incandescent IR lamp as the heat source, the holder on which the ITO substrate resides on, can be used to manipulate the substrate temperature.

IR lamp annealing using 125 W incandescent infrared light bulb was first tried. Sample substrates with perovskite layer on the top were placed on a supporting plate, which can be metal, wood, or glass. Fig. 37 shows the sample temperature versus annealing (radiation) time. When sample substrates were placed on the wood holding plate, it takes 5 minutes (300 seconds) for samples to reach 100 °C, which is required annealing temperature for perovskite thin films^[104]. However, when sample substrates were placed on either metal or glass holding plate, in 5 minutes their temperature can only reach about 43 °C and 60 °C, respectively, far away from required 100 °C annealing temperature.

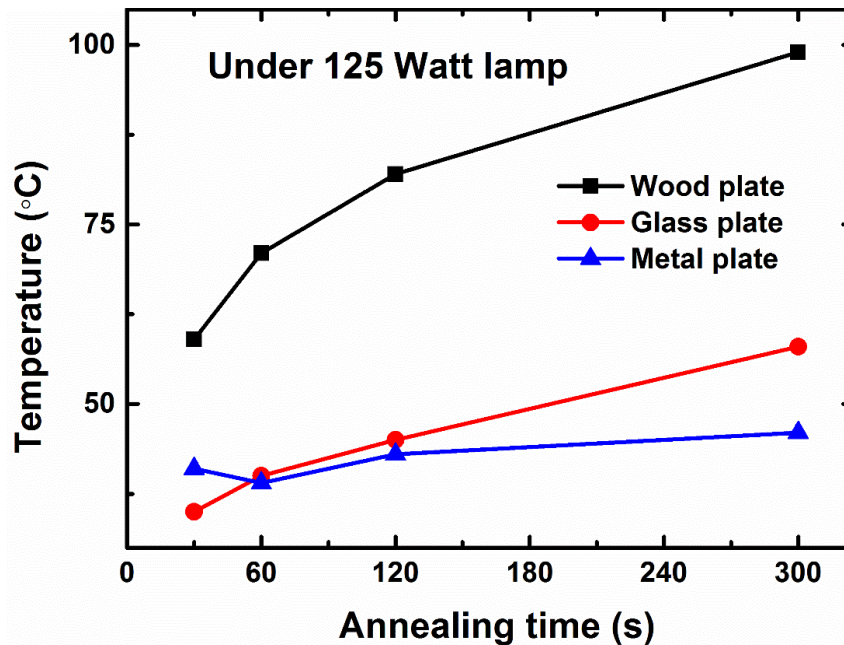


Figure 37: Sample temperature versus lamp annealing time under 125 W lamp when placed on wood, metal and glass sample supporting plate.

Then the 125 W lamp was replaced by a 250 W light bulb for doubled output power. The sample temperatures at different annealing times under radiation of 250 W

lamp are shown in fig. 38. Sample temperature increases quickly when these samples are placed on wood holding plate and it only takes 30 seconds for samples to reach aimed annealing temperature of 100 °C. As annealing time increases, the temperature for samples placed on either metal or glass supporting plate increases a little bit slower. It takes 1 minute and 3 minutes for samples on metal and glass holding plate to reach 100 °C, respectively.

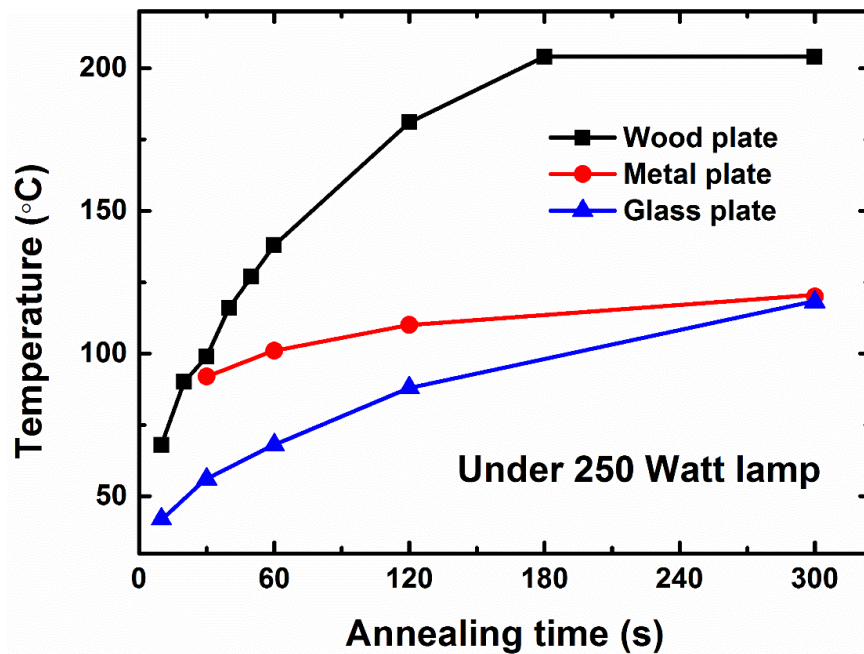


Figure 38: Sample temperature versus lamp annealing time under 250 W lamp when placed on wood, metal and glass sample supporting plate.

As shown in fig. 37 and 38, the material of the holder does matter for the heating results in lamp annealing. In this study, iron, glass and wood plates with thermal conductivity of ~ 80, 1 and 0.1 W/(mK), respectively, are used for comparison of heating temperature. The wooden plate gives much faster and higher annealing temperatures than iron and transparent glass holders. This can be attributed to that wood has a much lower

thermal conductivity than that of the iron and glass, plus it is opaque and does not allow radiation to pass through. The sample temperature increase on iron and glass plates shares the similar trend and is close to each other. It is hard for the produced thermal energy to be accumulated on iron plate because of its high thermal conduction for heat dissipation. On the other hand, although glass has much lower thermal conductivity, its transparency spares part of the incoming radiation energy, resulting in less generation of heat and slow temperature increase.

5.2 Morphology and crystallization of perovskite thin films, and resulting performance of perovskite solar cells

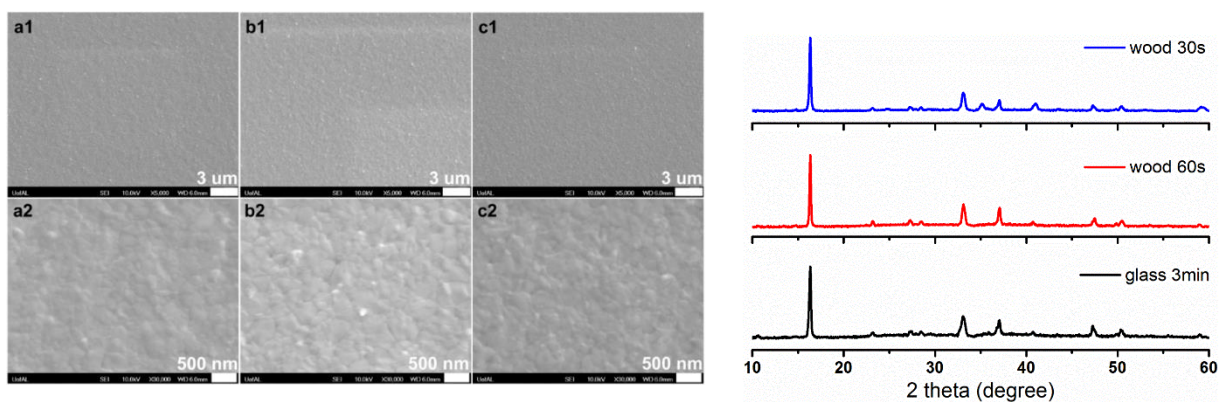


Figure 39: (Left) SEM images show morphologies of perovskite thin films with IR lamp annealing. (a) 30 seconds for samples on wood plate, (b) 60 seconds also on wood plate, (c) 3 minutes on glass sample holder. (Right) Corresponding XRD spectra.

The SEM images on left of fig. 39 reveal that all the perovskite films present good morphology after lamp annealing, and no morphology differences are observed among samples placed on different supporting plates. Note that all films were washed by toluene during spin coating process. Based on the XRD spectra shown in fig. 39b, only perovskite

characteristic peaks ($2\theta = \sim 15.5^\circ, 33.5^\circ, 37^\circ$) are observed, no peaks from PbI_2 ($2\theta = \sim 14.6^\circ$) and MAI ($2\theta = \sim 12.0^\circ$) precursors appear, indicating complete conversion of precursors into perovskite in rapid lamp annealing^[105].

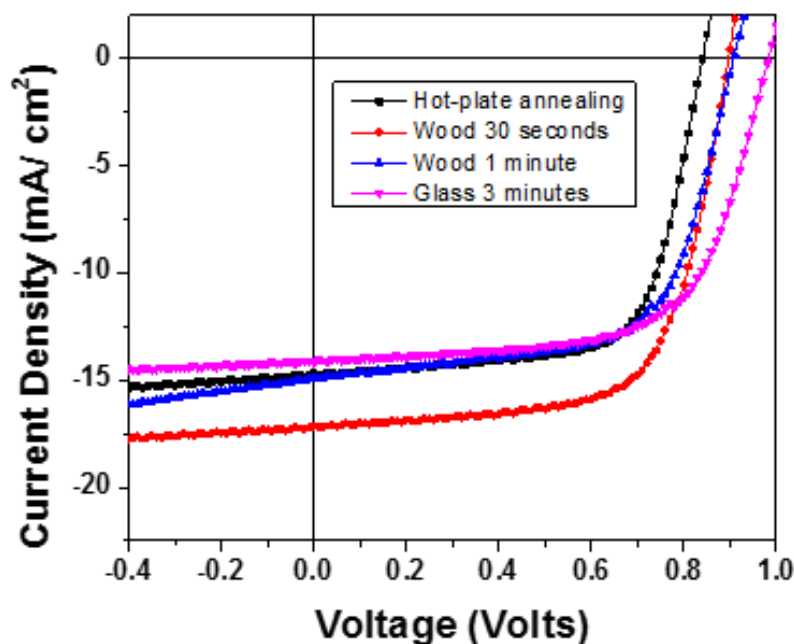


Figure 40: Comparison of I-V characteristics between fast lamp annealing in less than 3 minutes

The performance of the PSCs by means of current density versus voltage (J-V) measurements under simulated air mass (AM) 1.5 G (100 mWcm^{-2}) irradiation in ambient air was evaluated. Fig. 40 shows the J-V characteristics of perovskite solar cells with lamp annealing in less than 3 minutes and hot plate annealing for 1 hour. No significant differences in device performance were observed. It is noticed that perovskite solar cells with lamp annealing of 30 seconds on wood plate show slightly better performance with PCE of 10.3% than hot plate annealing for 1 hour with PCE of 9.0%. That is, rapid lamp annealing could somewhat improve efficiency while significantly reducing the annealing

time. Table 5 lists device parameters extracted from J-V characteristics, including power-conversion efficiency.

Table 5: Extracted device parameters from J-V characteristics in fig. 40

	PCE (%)	FF	Voc (V)	Jsc (mA/cm ²)
Hot-plate annealing (60 minutes)	9.0	70.49	0.84	15.13
IR lamp annealing (wood, 30 seconds)	10.3	68.439	0.88	17.14
IR lamp annealing (wood, 1 minute)	8.6	64.45	0.9	14.88
IR lamp annealing (glass, 3 minutes)	9.1	65.91	0.97	14.17

In conclusion, a new approach was demonstrated for deposition of perovskite films by introducing (PAMAM dendrimers as an additive to control the growth and nucleation of the film. A novel approach to anneal perovskite film using an infrared lamp has been developed, which can rapidly heat sample substrates with great uniformity as compared with the traditional hot plate annealing method. The perovskite solar cells from 250 W infrared lamp annealing in less than 3 minutes show similar or slightly better device performance than reference samples from hot plate annealing for 60 minutes (optimal condition). Particularly, perovskite solar cells with rapid lamp annealing for 30 seconds on wood holder show efficiency of 10.3% as compared with PCE around 9.0% from hot plate annealing for 60 minutes. These results prove the effectiveness of infrared lamp annealing over hot plate heating. The facile polymer additive approach for the deposition of perovskite thin films can improve the device stability without any encapsulation.

CHAPTER 6. CONCLUSION AND FUTURE WORK

6.1 Conclusions

Organo-lead halide perovskites have been emerging as a promising material in photovoltaics because of their high absorption coefficient, high free charge mobility and long carrier life time thereby long diffusion length. Solar cells based on organic–inorganic hybrid perovskite (PSCs) have attracted extensive attention due to easy fabrication and low-cost solution processes. One of the keys to the fabrication of high-performance PSCs is the control of crystallinity and morphology of the perovskite film. In this dissertation study, a controllable fabrication of annealing-free perovskite films with tunable crystal grain size and morphology via a seeded approach has been developed. Specifically, a solution of PbI_2 was spin-coated on a substrate, and a low concentration solution of MAI was dropped onto the PbI_2 film to form perovskite seed before introducing high concentration solution of MAI. The fast, annealing-free seeded nucleation and growth leads to dense and uniform perovskite thin films exhibited controllable crystal grains. This seeded crystallization technique offers a way to better control the device fabrication without the necessity of thermal annealing, which will boost the low-cost manufacture of efficient and reproducible PSCs.

In another project, a polymer additive assisted approach to facilitate the growth of uniform, dense, and ultra-smooth perovskite thin films has also been demonstrated. In specific, a polymer, PAMAM dendrimers, was incorporated into the blend solution of PbI_2

and MAI to regulate the nucleation and growth thereby tuning the morphology and crystallinity of the perovskite thin films. The PAMAM addition not only realized compact perovskite thin films without pinholes in it, but also increased the stability. This polymer additive assisted one-step method represents a facile route for the controllable fabrication of perovskite thin films and large-scale production of efficient and stable perovskite solar cells.

In the simulation study, both the organic bulk heterojunction solar cells and perovskite solar cells have been systematically investigated to help understanding device operation and guide the experiment. For perovskite solar cells, the effects of hole transport layer mobility and ITO anode work function on device performance have been investigated. As the hole mobility increases, the recombination is reduced thereby increasing the efficiency. Increase of ITO anode work function facilitates hole injection, leading to enhancement of performance. The simulation study of organic polymer solar cells includes optimization of active layer thickness and its dependence on charge carrier mobility and recombination rate, and influence of hole mobility in electron-donating polymer and different electron transport materials on power-conversion efficiency.

6.2 Future Work

Although much of the focus has been on improving the efficiency of the organic-halide perovskite solar cells, degradation of these cells has been much of a concern. As demonstrated in Chapter 5, incorporation of PAMAM impressively inhibited the color change, leading to significant enhancement of film stability. The more the PAMAM are loaded, less color change was observed, indicating more stable perovskite films. PAMAM

dendrimers have been characterized into various generations depending on the molecular weight, chain length and the side groups. For each increasing generation, molecular weight is almost doubled and produces larger molecular diameters. It is anticipated that with increase of PAMAM size, i.e., from low generation G1 to high generation G5, the increased density of nucleation seeds could result in dense film but small crystal sizes. Condensed film with PAMAM wrapped perovskite crystals could prevent the penetration of moisture or oxygen and protect the defect-rich crystal surface. In the further study, the correlation between PAMAM size and device performance including both efficiency and stability can be systematically investigated.

To study and compare the films morphology, crystallinity, stability and device performance with addition of different generation of PAMAM dendrimers, AFM can be used to analyze the surface roughness of the films, and SEM can be performed to study the surface morphology and cross-sectional SEM for layer by layer details of the fabricated device. Through cross-sectional SEM, the interfacial boundaries and the thickness of the individual layers can be determined. In addition, XRD and UV visible analysis can be carried out for in-depth study of the crystallinity and light absorption, respectively.

Large scale manufacturing of perovskite solar cells using low-cost high-speed printing techniques would be a huge leap toward practical applications. Among scalable roll-to-roll (R2R) printing technologies, slot-die coating has been demonstrated to be most successful in organic photovoltaics and various printed electronics.^[106–110] As an outstanding candidate, slot-die coating provides many advantages, including excellent film uniformity, precise thickness control in tens of nanometers, capable of processing a

wide range of fluids with high and low viscosity, reliable and robust process for high-yield mass production. Particularly, as one of great features different from other R2R coating techniques, slot-die coating deposits almost all the fluid onto the substrate (~95% material utilization), no recycling and purification of ink material are required. In addition, since slot-die coating is in a closed system, no fluid contamination to the environment is presented, which is important to prevent pollution of lead from perovskite materials.

As another future project, the developed and demonstrated new techniques, such as incorporation of PAMAM dendrimers to improve the crystallinity and control the stability of the perovskite film, can be integrated into roll-to-roll slot die coating on flexible substrates, achieving manufacturing of highly stable flexible perovskite solar cells for large scale production.

REFERENCES

- [1] U. S. E. I. Administration, *decembermonthlyenergyreview*.
- [2] J. You, Z. Hong, Y. M. Yang, Q. Chen, M. Cai, T. Song, C. Chen, **2014**.
- [3] O. Malinkiewicz, A. Yella, Y. H. Lee, G. M. Espallargas, M. Graetzel, M. K. Nazeeruddin, H. J. Bolink, *Nat. Photonics* **2013**, 8, 128.
- [4] N. Park, *J. Phys. Chem. Lett.* **2013**.
- [5] M. A. Loi, J. C. Hummelen, *Nat. Mater.* **2013**, 12, 1087.
- [6] a. Filippetti, A. Mattoni, *Phys. Rev. B* **2014**, 89, 125203.
- [7] Y. Li, C. Lin, G. Zheng, Z. Cheng, *Chem. ...* **2006**, 3463.
- [8] S. Kazim, M. K. Nazeeruddin, M. Grätzel, S. Ahmad, *Angew. Chem. Int. Ed. Engl.* **2014**, 53, 2812.
- [9] H. Zhou, Q. Chen, G. Li, S. Luo, T. -b. Song, H.-S. Duan, Z. Hong, J. You, Y. Liu, Y. Yang, *Science (80-.)*. **2014**, 345, 542.
- [10] L. Meng, J. You, T. F. Guo, Y. Yang, *Acc. Chem. Res.* **2016**, 49, 155.
- [11] B. Conings, L. Baeten, C. De Dobbelaere, J. D'Haen, J. Manca, H.-G. Boyen, *Adv. Mater.* **2013**, 2041.
- [12] Z. Xiao, C. Bi, Y. Shao, Q. Dong, Q. Wang, Y. Yuan, C. Wang, Y. Gao, J. Huang, *Energy Environ. Sci.* **2014**, 7, 2619.
- [13] J. You, Y. (Michael) Yang, Z. Hong, T.-B. Song, L. Meng, Y. Liu, C. Jiang, H. Zhou, W.-H. Chang, G. Li, Y. Yang, *Appl. Phys. Lett.* **2014**, 105, 183902.
- [14] Q. Wu, T. Van Voorhis, D. G. Nocera, D. G. Nocera, A. Bansal, J. A. Turner, M. Kapur, R. C. Kainthla, J. O. M. Bockris, J. A. Turner, E. L. Miller, A. Misra, T. L. Gibson, N. A. Kelly, S. C. Gau, O. J. Murphy, M. Kapur, J. O. M. Bockris, D. G. Nocera, M. W. Kanan, D. G. Nocera, Y. Surendranath, D. G. Nocera, M. Dinc, D. G. Nocera, Y. Surendranath, S. Y. Reece, D. G. Nocera, J. A. Gascon, J. P. Mcevoy, G. W. Brudvig, V. S. Batista, K. Kawakami, N. Kamiya, Y. Surendranath,

- D. A. Lutterman, D. G. Nocera, K. S. Choi, K. S. Choi, J. Sun, H. Inumaru, D. R. Gamelin, D. R. Gamelin, M. Cornuz, K. Sivula, D. R. Gamelin, E. A. Schiff, A. Luque, S. Hegedus, U. S. G. Survey, **2011**, 648.
- [15] M. Granstrom, K. Petritsch, a C. Arias, a Lux, M. R. Andersson, R. H. Friend, *Nature* **1998**, 395, 257.
- [16] B. P. Rand, J. Genoe, P. Heremans, J. Poortmans, *Prog. Photovolt Res. Appl.* **2015**, 15, 659.
- [17] T. Brown, J. Kim, R. Friend, F. Cacialli, R. Daik, W. Feast, *Appl. Phys. Lett.* **1999**, 75, 1679.
- [18] F. C. Krebs, *Sol. Energy Mater. Sol. Cells* **2008**, 92, 685.
- [19] K. W. Wong, H. L. Yip, Y. Luo, K. Y. Wong, W. M. Lau, K. H. Low, H. F. Chow, Z. Q. Gao, W. L. Yeung, C. C. Chang, *Appl. Phys. Lett.* **2002**, 80, 2788.
- [20] C. J. Brabec, S. E. Shaheen, C. Winder, N. S. Sariciftci, P. Denk, *Appl. Phys. Lett.* **2002**, 80, 1288.
- [21] J. a Christians, R. C. M. Fung, P. V Kamat, *J. Am. Chem. Soc.* **2014**, 136, 758.
- [22] E. Wasylishen, M. A. White, T. Stanley, J. M. Michiel, **1989**, 3.
- [23] I. Borriello, G. Cantele, D. Ninno, *Phys. Rev. B* **2008**, 77, 235214.
- [24] P. W. Liang, C. Y. Liao, C. C. Chueh, F. Zuo, S. T. Williams, X. K. Xin, J. Lin, A. K. Y. Jen, *Adv. Mater.* **2014**, 26, 3748.
- [25] G. Niu, X. Guo, L. Wang, *J. Mater. Chem. A* **2015**, Advance.
- [26] M. Grätzel, *Nat. Mater.* **2014**, 13, 838.
- [27] G. Niu, W. Li, F. Meng, L. Wang, H. Dong, Y. Qiu, *J. Mater. Chem. A* **2014**, 2, 705.
- [28] Q. Dong, Z. Wang, K. Zhang, H. Yu, P. Huang, X. Liu, Y. Zhou, N. Chen, B. Song, *Nanoscale* **2016**, 5552.
- [29] C. Chueh, C. Liao, F. Zuo, S. T. Williams, P. Liang, A. K.-Y. Jen, *J. Mater. Chem. A* **2015**, 3, 9058.
- [30] J. H. Heo, D. H. Song, H. J. Han, S. Y. Kim, J. H. Kim, D. Kim, H. W. Shin, T. K. Ahn, C. Wolf, T. W. Lee, S. H. Im, *Adv. Mater.* **2015**, 27, 3424.

- [31] C. Sun, Q. Xue, Z. Hu, Z. Chen, F. Huang, H. L. Yip, Y. Cao, *Small* **2015**, *11*, 3344.
- [32] C. Zuo, L. Ding, *Nanoscale* **2014**, *6*, 9935.
- [33] C. Y. Chang, C. Y. Chu, Y. C. Huang, C. W. Huang, S. Y. Chang, C. A. Chen, C. Y. Chao, W. F. Su, *ACS Appl. Mater. Interfaces* **2015**, *7*, 4955.
- [34] X. Li, M. I. Dar, C. Yi, J. Luo, M. Tschumi, S. M. Zakeeruddin, M. K. Nazeeruddin, H. Han, M. Grätzel, *Nat. Chem.* **2015**, *7*, 703.
- [35] B. C. Thompson, J. M. J. Fréchet, *Angew. Chem. Int. Ed. Engl.* **2008**, *47*, 58.
- [36] P. Peumans, A. Yakimov, S. R. Forrest, *J. Appl. Phys.* **2003**, *93*, 3693.
- [37] G. Yu, J. Gao, J. C. Hummelen, F. Wudl, A. J. Heeger, 1789.
- [38] G. Li, R. Zhu, Y. Yang, *Nat. Photonics* **2012**, *6*, 153.
- [39] B. R. Saunders, M. L. Turner, *Adv. Colloid Interface Sci.* **2008**, *138*, 1.
- [40] L. Dou, J. You, Z. Hong, Z. Xu, G. Li, R. a Street, Y. Yang, *Adv. Mater.* **2013**, *25*, 6642.
- [41] Y. Li, *Acc. Chem. Res.* **2012**, *45*, 723.
- [42] M. a. Brady, G. M. Su, M. L. Chabiny, *Soft Matter* **2011**, *7*, 11065.
- [43] Y. Yang, H. Zhong, Z. Bai, B. Zou, Y. Li, G. D. Scholes, **2012**.
- [44] S. Shaheen, *SPIE Newsroom* **2007**, *2*.
- [45] C. Deibel, V. Dyakonov, *Rep. Prog. Phys.* **2010**, *73*, 1.
- [46] G. D. Cauble, **2011**, 1.
- [47] Y. Min Nam, J. Huh, W. Ho Jo, *Sol. Energy Mater. Sol. Cells* **2010**, *94*, 1118.
- [48] J. Burschka, N. Pellet, S.-J. Moon, R. Humphry-Baker, P. Gao, M. K. Nazeeruddin, M. Grätzel, *Nature* **2013**, *499*, 316.
- [49] J. H. Heo, S. H. Im, J. H. Noh, T. N. Mandal, C. Lim, J. A. Chang, Y. H. Lee, H. Kim, A. Sarkar, K. Nazeeruddin, M. Gra, **2013**, 1.
- [50] H.-S. Kim, C.-R. Lee, J.-H. Im, K.-B. Lee, T. Moehl, A. Marchioro, S.-J. Moon, R. Humphry-Baker, J.-H. Yum, J. E. Moser, M. Grätzel, N.-G. Park, *Sci. Rep.* **2012**, *2*, 591.

- [51] A. Kojima, K. Teshima, Y. Shirai, T. Miyasaka, *J. Am. Chem. Soc.* **2009**, *131*, 6050.
- [52] M. M. Lee, J. Teuscher, T. Miyasaka, T. N. Murakami, H. J. Snaith, *Science* **2012**, *338*, 643.
- [53] M. Liu, M. B. Johnston, H. J. Snaith, *Nature* **2013**, *501*, 395.
- [54] S. D. Stranks, G. E. Eperon, G. Grancini, C. Menelaou, M. J. P. Alcocer, T. Leijtens, L. M. Herz, A. Petrozza, H. J. Snaith, *Science* **2013**, *342*, 341.
- [55] G. Xing, N. Mathews, S. S. Lim, Y. M. Lam, S. Mhaisalkar, T. C. Sum, **2013**, *6960*, 498.
- [56] Z. Xiao, C. Bi, Y. Shao, Q. Dong, Q. Wang, Y. Yuan, C. Wang, Y. Gao, *1*, 4.
- [57] A. Dualeh, N. Tétreault, T. Moehl, P. Gao, M. K. Nazeeruddin, M. Grätzel, *Adv. Funct. Mater.* **2014**, *In Press*.
- [58] Y. Wu, A. Islam, X. Yang, C. Qin, J. Liu, K. Zhang, W. Peng, L. Han, *Energy Environ. Sci.* **2014**, *7*, 2934.
- [59] M. J. Carnie, C. Charbonneau, M. L. Davies, J. Troughton, T. M. Watson, K. Wojciechowski, H. Snaith, D. A. Worsley, *Chem. Commun.* **2013**, *49*, 7893.
- [60] S. Lv, S. Pang, Y. Zhou, N. P. Padture, H. Hu, L. Wang, X. Zhou, H. Zhu, L. Zhang, C. Huang, G. Cui, *Phys. Chem. Chem. Phys.* **2014**, *16*, 19206.
- [61] M. M. Tavakoli, L. Gu, Y. Gao, C. Reckmeier, J. He, A. L. Rogach, Y. Yao, Z. Fan, *Sci. Rep.* **2015**, *5*, 14083.
- [62] D. Wang, Z. Liu, Z. Zhou, H. Zhu, Y. Zhou, C. Huang, Z. Wang, H. Xu, Y. Jin, B. Fan, S. Pang, G. Cui, *Chem. Mater.* **2014**, *26*, 7145.
- [63] J. Burschka, N. Pellet, S.-J. Moon, R. Humphry-Baker, P. Gao, M. K. Nazeeruddin, M. Grätzel, *Nature* **2013**, *499*, 316.
- [64] L. Hu, J. Peng, W. Wang, Z. Xia, J. Yuan, J. Lu, *ACS Photonics* **2014**, *1*, 547.
- [65] S. a. Kulkarni, T. Baikie, P. P. Boix, N. Yantara, N. Mathews, S. Mhaisalkar, *J. Mater. Chem. A* **2014**, *2*, 9221.
- [66] Q. Chen, H. Zhou, Z. Hong, S. Luo, H.-S. Duan, H.-H. Wang, Y. Liu, G. Li, Y. Yang, *J. Am. Chem. Soc.* **2014**, *136*, 622.

- [67] H. Hu, D. Wang, Y. Zhou, J. Zhang, S. Lv, S. Pang, X. Chen, Z. Liu, N. P. Padture, G. Cui, *RSC Adv.* **2014**, *4*, 28964.
- [68] C. Wehrenfennig, M. Liu, H. J. Snaith, M. B. Johnston, L. M. Herz, *Energy Environ. Sci.* **2014**, *7*, 2269.
- [69] Z. Liu, E.-C. Lee, *Org. Electron.* **2015**, *24*, 101.
- [70] N. J. Jeon, J. H. Noh, Y. C. Kim, W. S. Yang, S. Ryu, S. Il Seok, *Nat. Mater.* **2014**, *13*, 1.
- [71] Y. Rong, Z. Tang, Y. Zhao, X. Zhong, S. Venkatesan, H. Graham, M. Patton, Y. Jing, A. M. Guloy, Y. Yao, *Nanoscale* **2015**, *7*, pp 10595.
- [72] M. Lv, X. Dong, X. Fang, B. Lin, S. Zhang, J. Ding, N. Yuan, *RSC Adv.* **2015**, *5*, 20521.
- [73] P. Fedeli, F. Gazza, D. Calestani, P. Ferro, T. Besagni, A. Zappettini, G. Calestani, E. Marchi, P. Ceroni, R. Mosca, *J. Phys. Chem. C* **2015**, *119*, 21304.
- [74] N. J. Jeon, J. H. Noh, W. S. Yang, Y. C. Kim, S. Ryu, J. Seo, S. Il Seok, *Nature* **2015**, *517*, 476.
- [75] B. Saparov, D. B. Mitzi, *Chem. Rev.* **2016**, *116*, 4558.
- [76] W. Wang, M. O. Tade, Z. Shao, *Chem. Soc. Rev.* **2015**, *44*, 5371.
- [77] Y. Zhao, K. Zhu, *Chem. Soc. Rev.* **2015**, *45*, 655.
- [78] K. M. Boopathi, M. Ramesh, T.-Y. Huang, W. Budiawan, M. Y. Lin, C.-H. Lee, K.-C. Ho, C. W. Chu, *J. Mater. Chem. A* **2016**, *4*, 1591.
- [79] C. Bi, Q. Wang, Y. Shao, Y. Yuan, Z. Xiao, J. Huang, *Nat. Commun.* **2015**, *6*, 7747.
- [80] B. Li, J. Tian, L. Guo, C. Fei, T. Shen, X. Qu, G. Cao, *ACS Appl. Mater. Interfaces* **2016**, *8*, 4684.
- [81] Q. Liang, J. Liu, Z. Cheng, Y. Li, L. Chen, R. Zhang, J. Zhang, Y. Han, *J. Mater. Chem. A* **2016**, *4*, 223.
- [82] Y. Yang, C. Sun, H. L. Yip, R. Sun, X. Wang, *Chem. - An Asian J.* **2016**, *11*, 893.
- [83] Y. Zhou, O. S. Game, S. Pang, N. P. Padture, *J. Phys. Chem. Lett.* **2015**.
- [84] G. E. Eperon, V. M. Burlakov, P. Docampo, A. Goriely, H. J. Snaith, *Adv. Funct. Mater.* **2014**, *24*, 151.

- [85] W. Nie, H. Tsai, R. Asadpour, J.-C. Blancon, A. J. Neukirch, G. Gupta, J. J. Crochet, M. Chhowalla, S. Tretiak, M. A. Alam, H.-L. Wang, A. D. Mohite, *Science* (80-.). **2015**, *347*, 522.
- [86] S. T. Williams, F. Zuo, C.-C. Chueh, C.-Y. Liao, P.-W. Liang, A. K.-Y.-Y. K.-Y. Jen, *ACS Nano* **2014**, *8*, 10640.
- [87] B. Cai, W. H. Zhang, J. Qiu, *Cuihua Xuebao/Chinese J. Catal.* **2015**, *36*, 1183.
- [88] Y. Zhou, M. Yang, W. Wu, A. L. Vasiliev, K. Zhu, N. P. Padture, *J. Mater. Chem. A* **2015**, *3*, 8178.
- [89] W. Peng, B. Anand, L. Liu, S. Sampat, B. E. Bearden, A. Malko, Y. J. Chabal, *Nanoscale* **2015**, 1627.
- [90] Z. Song, S. C. Wathage, A. B. Phillips, B. L. Tompkins, R. J. Ellingson, M. J. Heben, *Chem. Mater.* **2015**, *27*, 4612.
- [91] H. Gao, C. Bao, F. Li, T. Yu, J. Yang, W. Zhu, X. Zhou, G. Fu, Z. Zou, *ACS Appl. Mater. Interfaces* **2015**, *7*, 9110.
- [92] G. E. Eperon, S. N. Habisreutinger, T. Leijtens, B. J. Bruijnaers, J. J. van Franeker, D. W. DeQuilettes, S. Pathak, R. J. Sutton, G. Grancini, D. S. Ginger, R. A. J. Janssen, A. Petrozza, H. J. Snaith, *ACS Nano* **2015**, *348*, 150806144801005.
- [93] X. Gong, M. Li, X.-B. Shi, H. Ma, Z.-K. Wang, L.-S. Liao, *Adv. Funct. Mater.* **2015**.
- [94] M. Zhang, H. Yu, M. Lyu, Q. Wang, J.-H. Yun, L. Wang, *Chem. Commun.* **2014**, *50*, 11727.
- [95] Y. Ogomi, A. Morita, S. Tsukamoto, T. Saitho, N. Fujikawa, Q. Shen, T. Toyoda, K. Yoshino, S. S. Pandey, S. Hayase, **2014**.
- [96] A. Sadhanala, F. Deschler, T. H. Thomas, S. E. Dutton, K. C. Goedel, F. C. Hanusch, M. L. Lai, U. Steiner, T. Bein, P. Docampo, D. Cahen, R. H. Friend, *J. Phys. Chem. Lett.* **2014**, 140709102712008.
- [97] Y. Xie, F. Shao, Y. Wang, T. Xu, D. Wang, F. Huang, *ACS Appl. Mater. Interfaces* **2015**, *7*, 12937.
- [98] X. Song, W. Wang, P. Sun, W. Ma, Z. K. Chen, *Appl. Phys. Lett.* **2015**, *106*.
- [99] J. H. Heo, H. J. Han, D. Kim, T. K. Ahn, S. H. Im, *Energy Environ. Sci.* **2015**, *8*, 1602.

- [100] H.-L. Hsu, C.-C. Chang, C.-P. Chen, B.-H. Jiang, R.-J. Jeng, C.-H. Cheng, *J. Mater. Chem. A* **2015**, *3*, 9271.
- [101] J. H. Heo, S. H. Im, *Phys. Status Solidi - Rapid Res. Lett.* **2014**, *8*, 816.
- [102] G. Li, T. Zhang, Y. Zhao, *J. Mater. Chem. A* **2015**, *3*, 19674.
- [103] Y. Zhang, X. Hu, L. Chen, Z. Huang, Q. Fu, Y. Liu, L. Zhang, Y. Chen, *Org. Electron. physics, Mater. Appl.* **2016**, *30*, 281.
- [104] N. Ahn, D. Y. Son, I. H. Jang, S. M. Kang, M. Choi, N. G. Park, *J. Am. Chem. Soc.* **2015**, *137*, 8696.
- [105] C. Ying, C. Shi, N. Wu, J. Zhang, M. Wang, *Nanoscale* **2015**, *10*.
- [106] A. Sandström, H. F. Dam, F. C. Krebs, L. Edman, *Nat. Commun.* **2012**, *3*, 1002.
- [107] T. T. Larsen-Olsen, B. Andreasen, T. R. Andersen, A. P. L. Böttiger, E. Bundgaard, K. Norrman, J. W. Andreasen, M. Jørgensen, F. C. Krebs, *Sol. Energy Mater. Sol. Cells* **2012**, *97*, 22.
- [108] M. Helgesen, J. E. Carlé, F. C. Krebs, *Adv. Energy Mater.* **2013**, *3*, 1664.
- [109] T. R. Andersen, H. F. Dam, M. Hösel, M. Helgesen, J. E. Carlé, T. T. Larsen-Olsen, S. a. Gevorgyan, J. W. Andreasen, J. Adams, N. Li, F. Machui, G. D. Spyropoulos, T. Ameri, N. Lemaître, M. Legros, A. Scheel, D. Gaiser, K. Kreul, S. Berny, O. R. Lozman, S. Nordman, M. Välimäki, M. Vilkmann, R. R. Søndergaard, M. Jørgensen, C. J. Brabec, F. C. Krebs, *Energy Environ. Sci.* **2014**, *7*, 2925.
- [110] F. Liu, S. Ferdous, E. Schaible, A. Hexemer, M. Church, X. Ding, C. Wang, T. P. Russell, *Adv. Mater.* **2015**, *27*, 886.